12-2020

AN EXPERIMENTAL INVESTIGATION OF HIGH-SPEED AIR-BREATHING VEHICLE PERFORMANCE METRICS

Katherine M. Stamper
kstamper@vols.utk.edu

Recommended Citation

Stamper, Katherine M., "AN EXPERIMENTAL INVESTIGATION OF HIGH-SPEED AIR-BREATHING VEHICLE PERFORMANCE METRICS. " Master's Thesis, University of Tennessee, 2020.
https://trace.tennessee.edu/utk_gradthes/5857

To the Graduate Council:

I am submitting herewith a thesis written by Katherine M. Stamper entitled "AN EXPERIMENTAL INVESTIGATION OF HIGH-SPEED AIR-BREATHING VEHICLE PERFORMANCE METRICS." I have examined the final electronic copy of this thesis for form and content and recommend that it be accepted in partial fulfillment of the requirements for the degree of Master of Science, with a major in Aerospace Engineering.

John D. Schmisseur, Major Professor

We have read this thesis and recommend its acceptance:

Phillip A. Kreth, Trevor M. Moeller

Accepted for the Council:
Dixie L. Thompson

Vice Provost and Dean of the Graduate School

(Original signatures are on file with official student records.)

AN EXPERIMENTAL INVESTIGATION OF HIGH-SPEED AIR-BREATHING VEHICLE PERFORMANCE METRICS

A Thesis Presented for the
Master of Science
Degree
The University of Tennessee, Knoxville

Katherine Marilyn Stamper
December 2020

ACKNOWLEDGEMENTS

First, I would like to thank Computational Fluid Dynamics Research Corporation (CDRC) for funding a supporting this work under project number #9326. I would like to thank far too many people to list in this section. I would like to thank Dr. John Schmisseur for his continual support and belief in me, especially when I did not believe it myself. My committee, Dr. Phil Kreth and Dr. Trevor Moeller, who have helped shape me into the engineer I am today. Matthew Schwartz has not only been a computational counterpart, but also a dear friend. Also, I would like to thank Jack Cobourn for his support in the lab and in writing this thesis.

I would like to thank Jonathan Kolwyck, Jacob Bowman, and Joel Davenport for their support in running the Mach 2 wind tunnel. Gary Payne, Kirk Davenport, and Jack LeGeune have shared so much of their expertise in machining and design with me. The UTSI Administration and faculty have been so influential in my time here.

So many friends and coworkers have made this graduate school experience such a great opportunity. I would like to thank the entire HORIZON Research Group, members past and present, for their continual professional, academic, and emotional support. I would like to tank my fellow HORIZON interns in Summer 2017 as well as all the interns I have mentored since then. I am so grateful for the opportunity to intern as NASA Ames Research Center and meet the incredible staff and interns there. I would also like to thank my Duck River Dance and Millennium Repertory family for their continual support and creating a home for me here in Manchester.

Finally, I would like to thank my family for without who I would not have made it to the end of this journey. To my Woods Reservoir rescues, the sweetest cats, Rey and Finn who will always cuddle and remind me of my time here.

ABSTRACT

High-speed air-breathing vehicles are one of the main hypersonic vehicles currently being developed. There is a current push by major world powers to develop these vehicles and one of the major limiting factors is engine design. The high-speed air-breathing vehicles necessitate an engine that can perform at higher speeds and higher temperatures, such as a scramjet. This engine is broken into three main parts: the inlet, isolator, and combustor. One of the primary concerns for these vehicles is engine unstart, which is when there is no longer supersonic flow through the engine and the engine can no longer perform. This is typically considered a worst-case scenario for these vehicles and is equated with vehicle loss.

This study is broken into two main experiments looking at the inlet and isolator sections of the scramjet flow path. These experiments were done with computational counterparts as the need for complementary studies has been well documented in the literature. Specifically for scramjets, the flight Mach number, Reynolds number, and enthalpy are very difficult to match in ground testing. Thus, there is a distinct need for computational studies to support ground testing in vehicle development.

The inlet study uses a crossing shock-wave/boundary-layer interaction as a canonical representation of an inlet, specifically at an off-design-condition with a large shock-wave/boundary layer created in the inlet flow. Then, vortex generators were employed to determine the effect of passive flow control on such an interaction. They were shown to delay separation but cause in increase in flow distortion.

The isolator study used a dynamic cylinder model to create a shock train in the wind tunnel test section. This accurately modeled a shock train in an isolator section of a scramjet flow path. Unstart was then created by moving the shock train with the dynamic cylinder which changed the backpressure ratio. Additionally, the asymmetrical nature of the shock train was investigated in the experimental data after the asymmetry was noted in the computations. The experimental data conferred well with the computational data as a strong asymmetrical trend was shown.

PREFACE

For a star to be born there is one thing that must happen: a gaseous nebula must collapse.

So collapse.
Crumble.
This is not your destruction.

This is your birth.

-Zoe Skylar

Each one of you can change the world, for you are made of star stuff, and you are connected to the universe.

-Vera Rubin

TABLE OF CONTENTS

Chapter One Introduction....1
  Motivation....1
  Objectives....4
  Research Questions....6
    Crossing Shock-Wave/Boundary Layer Interaction Experiment....6
    Unstart Experiment....6
  Mach 2 Wind Tunnel Facility....7
Chapter Two Crossing Shock-Wave/Boundary-Layer Experiment....9
  Literature Review....9
    CSWBLI....9
    Vortex Generators....13
  Experimental Set Up and Diagnostics....15
    Fins and Vortex Generator Model....15
    Surface Oil Flow Visualization Experimental Setup....18
    Pressure Transducers....18
  Results....18
    Oil Flow Results....22
    CFD Comparison....31
    Impact of the Sidewall Boundary Layer....37
    Uncertainty Analysis....43
Chapter Three Unstart Experiment....44
  Literature Review....44
    The Unstart Problem....44
    Shock Train Dynamics....46
  Experimental Set Up and Diagnostics....51
    Model and Actuator Design....51
    Full Diagnostic Set Up Suite....51
    Retroreflective Shadowgraphy....54
  Results....54
    Shock Train Generation....57
    Asymmetrical Nature of the Unstart Shock....57
    Uncertainty Analysis....72
Chapter Four Conclusion....74
  Crossing Shock-Wave/Boundary-Layer Interaction Experiment....74
  Unstart Experiment....75
List of References....76
Vita....81

LIST OF TABLES

Table 2.1. Test Matrix of Vortex Generator Configurations................................19
Table 2.2. Results of single VG cases compared to baseline. 28
Table 2.3. Comparison of quasi-conical structure between baseline and optimized VG cases...30
Table 2.4 Percent difference between the computational and experimental separation distance..34
Table 2.5. Comparison of fin generated SBLI quasi-conical structure 42

LIST OF FIGURES

Figure 1.1 Comparison of ISP for various vehicles at a range of Mach numbers. [11]....3
Figure 1.2. Diagram of a typical scramjet flow path and shock structure [17]. 5
Figure 1.3. Schematic of the UTSI Mach 2 Wind Tunnel. [25] 8
Figure 2.1. Crossing shock-wave/boundary layer interaction. [30]....10
Figure 2.2. Comparison of experimental oil flow and computational stream lines which show good agreement [30] 11
Figure 2.3 Footprint of the swept shock interaction. [34]....12
Figure 2.4. Localized flow effects of a vortex generator [38]....14
Figure 2.5. Optimized dimensions of a VG in supersonic flow [43] 16
Figure 2.6. Representative model schematic.....17
Figure 2.7. Oil mixture painted on the test section floor and illuminated by black light before a wind tunnel run.....20
Figure 2.8. Pressure transducer locations along the wind tunnel floor.....21
Figure 2.9. Case comparison between the baseline and all three VG cases.....23
Figure 2.10. Example of how separation distance was determined for the baseline case.....24
Figure 2.11. Separation distance from the leading edge of the fin normalized by the boundary layer height. 25
Figure 2.12. Single VG Cases. 27
Figure 2.13. Flow features of the conical structure interaction for the baseline case. 29
Figure 2.14. Pressure values for the different VG configurations both before and after the interaction.....32
Figure 2.15. Comparison of separation data for the experimental and CFD cases. CFD results from Ref. [21] and Ref. [22].....33
Figure 2.16. Experimental oil flow compared with computational streamlines for the baseline case. Flow is left to right. Simulations are from Ref. [21]....35
Figure 2.17. Experimental oil flow against computational streamlines for the VG case. Flow is left to right. [21] 36
Figure 2.18. Outlet stagnation pressures without VGs (left) and with VGs (right). Flow is into the page. From Ref. [21]....38
Figure 2.19. Oil flow image with false color of single fin SBLI with the influence of the sidewall boundary layer. 39
Figure 2.20. Oil flow of fin at 10° angle of attack in the UTSI Mach 2 wind tunnel. *Courtesy of Douthitt et al.* 40
Figure 2.21. Fin generated SBLI at 10°. [33]....41
Figure 3.1. Inlet of a SR 71 in unstarted and started conditions. [49]....45
Figure 3.2. Oscillation of unstart shock in little and big buzz mode. [51]....47
Figure 3.3. Nozzle starting at Mach 1.6 with asymmetric normal SBLI. [35] 48
Figure 3.4. Shock train structure [18]....49

Figure 3.5. Plot showing the type of shock train based on tunnel geometry and Mach number [18]. The UTSI Mach 2 facility has been added as the purple x. 50
Figure 3.6. Rendering of cylinder and ceiling insert. 52
Figure 3.7. Linear actuator mounted in the third test section. 53
Figure 3.8. Schematic shows the flow features that is created with the actuated model and imaging diagnostics. 55
Figure 3.9. Retroreflective shadowgraphy schematic. Adapted from Schwartz et al. 56
Figure 3.10. Image sequence showing the tunnel moving from a started to unstarted state at 50 Hz. Flow is left to right. 58
Figure 3.11. Image sequence showing the movement of the shock train at 10 kHz. Flow is left to right. 59
Figure 3.12. The starting shock of the wind tunnel with the centerline of the tunnel marked with an orange line. 60
Figure 3.13. The initial unstart shock as the tunnel moves to an unstart condition with the centerline of the tunnel marked with an orange line. 61
Figure 3.14. Measured flow features of the shock train for the asymmetry study. 63
Figure 3.15. Mach stem length versus time for the starting shock of the wind tunnel. 64
Figure 3.16. Mach stem height vs location in the wind tunnel shown as distance from the cylinder face. 65
Figure 3.17. The distance from the Mach stem midpoint from the centerline of the tunnel normalized by the tunnel half height. 66
Figure 3.18. Histogram of Mach stem midpoint to the centerline of the wind tunnel for the start data. 68
Figure 3.19. The Mach stem size versus location in the wind tunnel. 69
Figure 3.20. The distance of the Mach stem midpoint from the tunnel centerline normalized by the tunnel half height versus the location in the tunnel. 70
Figure 3.21. The distance of the Mach stem midpoint from the tunnel centerline normalized by the tunnel half height versus time. 71
Figure 3.22. Histogram of Mach Stem midpoint distance to the centerline for the unstart data set. 73

CHAPTER ONE

INTRODUCTION

Research is what you are doing when you do not know what you are doing. -Wernher Von Braun

Motivation

Hypersonic technology development is currently one of the highest Department of Defense priorities [1] [2]. A portion of this area of development focuses on vehicles that fly at hypersonic speeds. Hypersonic speed is defined generally as speeds above Mach 5, but in physics nothing of a fundamental nature changes between Mach 4.9 and 5.1 [3]. True hypersonic flows are flows where thermochemical effects and heating are significant factors. Since WWII, there has been a long boom/bust cycle in hypersonic research funding [4]. Hypersonic weapons can potentially change the nature of military operations due to their ability to drastically increase speed of response time, vehicle range, and survivability [5] [4] [1]. . As the need for global response in a limited time frame has increased, the development of hypersonic vehicles has become a priority for several nations and airbreathing systems are the focus of several technology maturation initiatives. The current push to develop weapons in the US follows reporting that China and Russia have had numerous successful hypersonic glide tests and are expected to have operational capabilities soon, creating a potential capability gap [1] [6] [7]. While it is a matter of debate if the technologies are as capable as claimed, hypersonic weapons have yet to be used [8] [7]. There is still a strong need for the US to be able to respond to this threat [6]. The push for the development of hypersonic vehicles as weapons between all three countries has all the classic characteristics of an arms race [6, 9].

The history of hypersonic vehicle development is one primarily of failure. Often, the biggest research accomplishment in these programs is determining what ‘unknown unknowns’ [4] [5]. Such as with the Hypersonic Ramjet Experiment in the mid-1960s [5], for which the goal was to develop a supersonic combustion ramjet (now known as a scramjet. The only critical accomplishment of the program was as John V Becker writes “the illumination of critical unknowns” [5]. Additionally, the X-15, the first experimental hypersonic aircraft, flying at a world record Mach 6.7, exposed the issues of shock/shock interactions after a test where an interaction burned off the pylon supporting a test ramjet engine [4] [10]. The tragic accident of the Columbia Space Shuttle in 2003 also highlights the complexity and unknowns of the hypersonic flow field [5].

Space access is one of the areas, in addition to military applications, where hypersonic reusable vehicles are a vital step for future development [4] [5]. The most well-known and successful hypersonic vehicle to date is NASA’s Space Shuttle. The Space Shuttle was the first attempt at a reusable vehicle to access space. Reentry is one of the major areas of hypersonic flows where reentry vehicle speeds can reach Mach 20 and above. Access to space will always require hypersonic flight [5]. While currently rockets are used to access space, the specific impulse (ISP), which shows how efficient a vehicle is at using fuel, of a scramjet is much higher than a rocket and would require less fuel and has no need to carry an oxidizer (i.e. less weight). Figure 1.1 shows the much larger ISP of a scramjet with either a hydrogen or hydrocarbon fuel source. Thus, scramjets can offer an economic alternative to primarily rocket based systems as scramjets cannot propel a vehicle into orbit or space. The Space Shuttle was initially conceived as a low-cost reusable system but was plagued with lengthy safety checks after each launch. [5]

Two main types of hypersonic vehicles are the current focus of hypersonic technology development: glide and cruise vehicles. Hypersonic glide vehicles are launched from a rocket and then glide to their target at extremely high speeds. Cruise missiles are those powered by high-speed air-breathing vehicles and will be the focus of this study [7]. While Russia and China are developing hypersonic vehicles to be tipped with nuclear warheads, the US is not [7] [9]. Thus, the US systems must be 10-100 times more accurate than that of our rivals which demands a much more difficult to develop system [7].

The focus of this study is primarily on hypersonic cruise vehicles, specifically the air-breathing propulsion systems. These vehicles use shock compression at high speeds to compress the air into the combustor. As flight speed increases, the heat in the combustor becomes too large for turbojets and ramjets, which are similar to scramjets but use subsonic air, to function adequately [5]. Thus, the shift to a scramjet is required to fly in these higher speed ranges. The advantages to this switch are the ability to fly at faster speeds with no moving parts, but there are new aerodynamics concerns in these engines.

The development of high-speed air breathing vehicles is a highly interdisciplinary problem combining the work of aerothermodynamics, propulsion, material science, flight controls, chemistry, and computational science [4] [5] [10] . Additionally, there are many key basic research fields which are still unknowns and are vital to the successful development of these vehicles. Specifically, in the aerothermodynamics field, these unknowns include boundary layer transition and shock-wave/boundary-layer interactions [4]. These vehicles are inherently difficult to study due to the highly integrated nature of the vehicle and the number of unknowns. Thermochemistry effects are difficult to match in ground test facilities [5]. Their flight range is at low altitude, which is difficult to study in a ground test environment. This flight range limits the effects of thermochemical nonequilibrium which is more of a factor at very high Mach numbers [4], but is an area where boundary layer transition may occur [5].

Since experimental studies can typically only match Mach number, Reynolds number, or total enthalpy, a greater reliance on computational methods is required for the development of these systems. Numerical simulations and ground testing together form the foundation on which flight vehicles are designed [4] and there is a large benefit in having joint computational and experimental studies. The importance of direct experimental and computational studies have been detailed by Dolling [11] , Settles and Dodson [12] , and Benek [13]. One of the difficulties in only having literature experimental data as comparison results in many parameters being unknown for computations as noted by Benek [13]. Having joint studies that include experimental validation allows for more accurate comparisons between computational and experimental data.

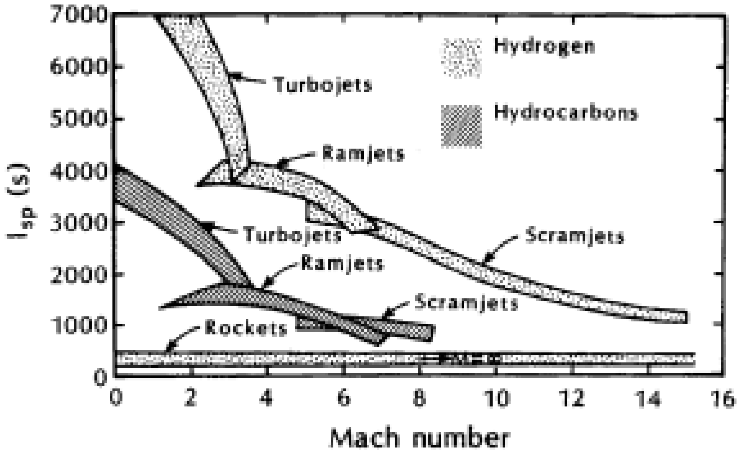

Figure 1.1 Comparison of ISP for various vehicles at a range of Mach numbers. [14]

The flow path through a scramjet engine can be seen below in Figure 1.2. from Ref [15]. As the vehicle flies, the air is captured by the inlet section of the vehicle and shocked down in speed by the initial bow shock of the vehicle as well as the shocks created by the inlet lip. One of the concerns stemming from shocks inside the inlet is shock-wave/boundary-layer interactions (SBLI). These can be seen on the image below as well. Shock wave/boundary-layer interactions are one of the driving factors of inlet design and the progression of hypersonic vehicles. They have been a focus of aerospace research since the 1960s and a variety of geometries have been studied, including cylinders, fins, and ramps [16] [11]. SBLI create thermal, acoustic, and pressure loads on a vehicle which, unchecked at high Mach numbers, potentially lead to local structural damage [16] [11].

The next section in the scramjet flow path is the isolator section which is dominated by the shock train. The shock train, while its own unique flow phenomena, is essentially a normal shock-wave/ boundary-layer interaction. This is the section that is traditionally studied when looking at the potential unstart of the vehicle [17]. Unstart has many possible definitions and causes as it is still a subject of great research [17]. Generally, unstart is characterized as when there is no longer supersonic flow in the engine and the shock train is ejected. This causes the engine to no longer operate and is considered a loss of the vehicle by the US government [18]. Thus, unstart needs to be extensively characterized and studied to prevent and mitigate an unstart event.

Objectives

The objective of this work is to understand key flow parameters in both the inlet and isolator sections of a scramjet flow path. For the inlet region, the flow will be modeled by a crossing shock-wave/boundary-layer interaction (CSWBLI). This represents an exaggerated version of the flow coming off the inlet and can be considered as a worst-case type scenario. The isolator section is physically represented by the square wind tunnel test section and a dynamic cylinder is used to change the area ratio and induce a shock train. The major research questions and scientific goals of these experiments are listed in the next section, following a general description of both experiments contained in this document.

Both experiments were performed in conjunction with computational counterparts [19] [20]. The importance of joint studies for scramjet research has already been discussed but having the ability to refer with computational counterparts in both studies led to a more refined experimental side of the study and answered additional questions as they were discovered.

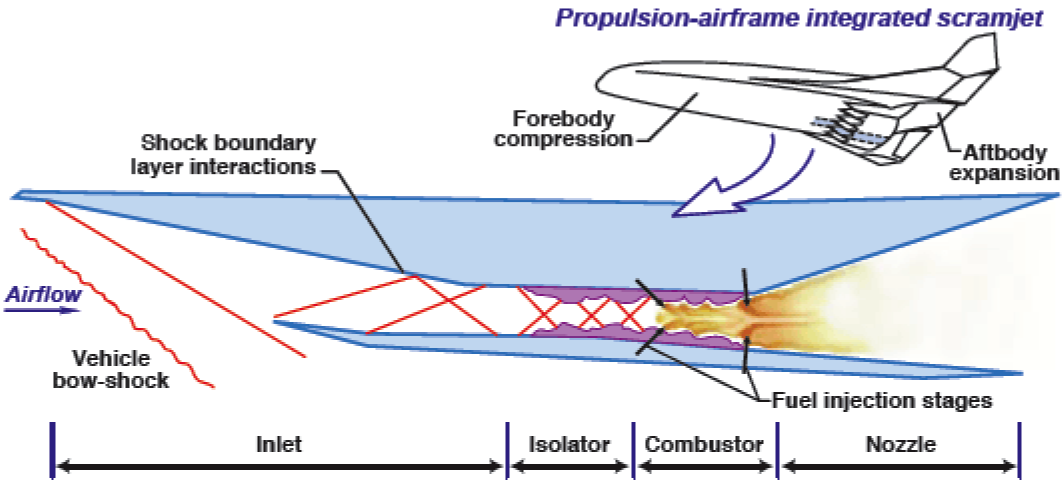

Figure 1.2. Diagram of a typical scramjet flow path and shock structure [21].

The CSWBLI study used the interaction to represent a worst-case inlet flow path where the addition of passive flow control would be beneficial. Vortex generators (VGs) were chosen as the form of passive flow control for this experiment and were used to try and push separation downstream. The experimental piece of this study was to determine the ideal arrangement of VG orientation and number to move separation downstream. This is one of the few cases when running multiple configurations experimentally was easier due to the very small size of the VGs which drastically increases computational expense. Then the computations replicated the experiments and determined the bulk flow effect of the VGs. Additionally, this was the first time the code Kestrel had been used on internal flows, so matching the baseline cases also show the validity of the code at computing internal flow [22].

The unstart experiment was a joint project with Computational Fluid Dynamics Research Cooperation (CFDRC) under project number 9326 to better understand the uncertainty quantification around unstart. The initial work shown in this study was to verify that the flow path of a shock train could be experimentally generated in the facility and the appropriate data could be gathered using non-intrusive diagnostic techniques. While this was only an initial experiment to prove validity, the data gathered also helped determine the asymmetrical nature of the shock train. This asymmetry was seen in the computations and was able to be further investigated in using the experimental data. This comparison is not something that can be as easily done when only referring to literature publications. Thus, the benefits of joint computational and experimental studies is shown.

Research Questions

The major research questions and experimental objectives for both studies are listed below. These drove the experimental design, test matrix, and determined when the experiments had reached their goals. These studies helped refine the computational parameters for the computational partners and again showed the benefit of the joint studies.

Crossing Shock-Wave/Boundary Layer Interaction Experiment

- Examine the effectiveness of vortex generators as passive flow control on a CSWBLI.
- Provide experimental validation for complimentary CFD experiments via streamlines and pressure data.
- Examine the impact of an incoming sidewall boundary layer to the fin generated interaction.

Unstart Experiment

- Determine if the shock train structure can be induced in the wind tunnel with a dynamic cylinder model.
- Characterize the asymmetrical nature of the unstart shock.

Mach 2 Wind Tunnel Facility

The Mach 2 wind tunnel at UTSI was used to simulate the scramjet flow path for both experiments. For the CSWBLI experiment, the inlet was modeled using two symmetrical sharp fins mounted to the tunnel sidewall. The inflow velocity to the inlet will be less than that in the freestream due to the effect of the bow shock [23]. For a vehicle traveling at Mach 5, the speed of the flow seen by the inlet would be closer to Mach 2. For the unstart experiment, the isolator will be modeled by the square test section and a dynamic cylinder was mounted at the end of the test section to model changes in back pressure. The design condition for an isolator is usually between Mach 1.5 and 2.5 [17], so the Mach 2 tunnel is generally consistent with the conditions for studying the isolator flow phenomena.

Additional factors also made the Mach 2 facility a good choice for modeling a scramjet flow path. The tunnel provides the appropriate Mach number, high Reynolds number, and the ability to run repeatedly for long amounts of time. This wind tunnel has a constant cross section of 203 mm × 203 mm (8” × 8”). The square test section is ideal for representing an isolator section [24]. Air is supplied as the test gas by a 23.6 m^3 bottle farm compressed to at most 20 MPa and the plenum pressure is maintained by a control valve at approximately 210 kPa. The storage tank pressure is sufficient to allow for run times up to two minutes, which is vital for the unstart experiments. The flow is not heated and the air is cooled by expansion through a mass flow control valve, resulting in stagnation temperatures of approximately 285 K. The freestream velocity is on average 507 m/s, resulting in a freestream Mach number of 2.01 and a freestream unit Reynolds number of approximately 3.0×10^7 m^{-1}. A turbulent boundary layer develops naturally along the floor of the wind tunnel with a thickness, δ, of approximately 11 mm in the first wind tunnel test section. [25] [26] Optical access for the experiments was provided by a BK7 glass window on the wind tunnel side walls and ceiling. The large amount of optical access in the sidewalls and the ceiling allowed for the visibility of the bulk flow field and optical diagnostics. The floor of the wind tunnel was visible via the sidewalls, but the ceiling is not visible due to tunnel design. A schematic of the Mach 2 wind tunnel can be seen in Figure 1.3.

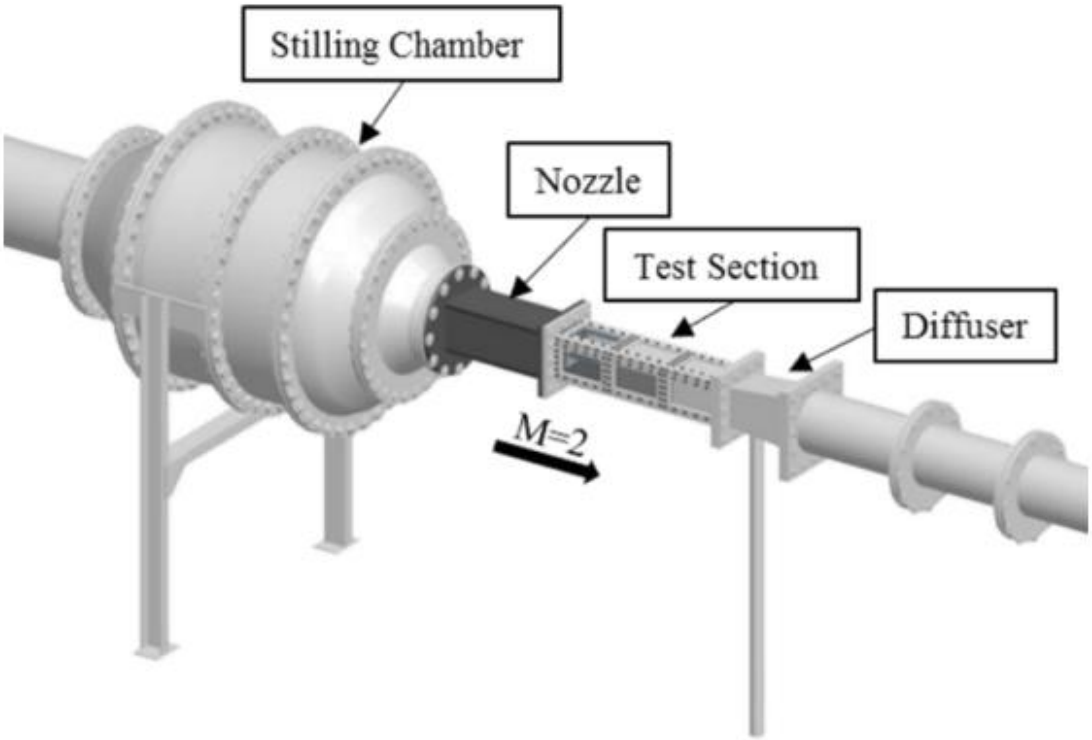

Figure 1.3. Schematic of the UTSI Mach 2 Wind Tunnel. [25]

CHAPTER TWO

CROSSING SHOCK-WAVE/BOUNDARY-LAYER EXPERIMENT

I had discovered that learning something, no matter how complex, wasn't hard when I had a reason to want to know it. — Homer Hickam, Rocket Boys

Literature Review

CSWBLI

As noted previously, SBLIs have been a focus of aerospace research since the 1960s and a variety of geometries have been studied, including cylinders, fins, and ramps [16] [11]. SBLI create thermal, acoustic, and pressure loads on a vehicle which, uncontrolled, could potentially lead to local damage [16] [11]. Specifically, for airbreathing vehicles, SBLI can lead to increased total pressure loses and flow [27]. This can lead to unstart in the inlet or cause significant damage to the structure due to the high thermal and pressure loads [28] [29]. SBLI continue to be a major area of research due to these factors.

A crossing shock-wave/boundary-layer interaction will be the main type of interaction in this study. The geometry of the shock generator and the shock structure can be seen in Figure 2.1. The double fin geometry creates a crossing shock interaction which simulates a supersonic inlet that has been studied numerically [30] and experimentally [28] [29] [31]. Historically, RANS simulations have been challenged to reproduce the features of these interactions. In the computational work of Schmisseur [30] and experimental work Zheltovodov [28], the increase in shock strength at higher Mach numbers and steeper angles of attack produced created more complex flow features but still showed agreement. More refined computational work, showed agreement with the experimental results, showing that the mean flow field could be captured numerically even for strong interactions [30]. An example of the numerical and experimental agreement for this particular shock structure can be seen in Figure 2.2, where computations were preformed to match the experimental results generated by oil flow. Current work for example the work being done by Adler et al. uses more computationally intensive methods such as LES to better resolve these flow fields [32].

While the CSWBLI is a unique flow structure, it bears a lot of similarities to the sharp fin generated SBLI. A sharp fin is a canonical configuration for studying 3D SBLI as seen in the work of Arora et al [33] and Figure 2.3. One of the main differences is a larger incoming boundary layer due to the fully developed boundary layer on the tunnel floor and a sidewall boundary layer that interacts with the leading edge of the fins. Additional analysis was done in this study to better characterize the effect of these changes on the interaction.

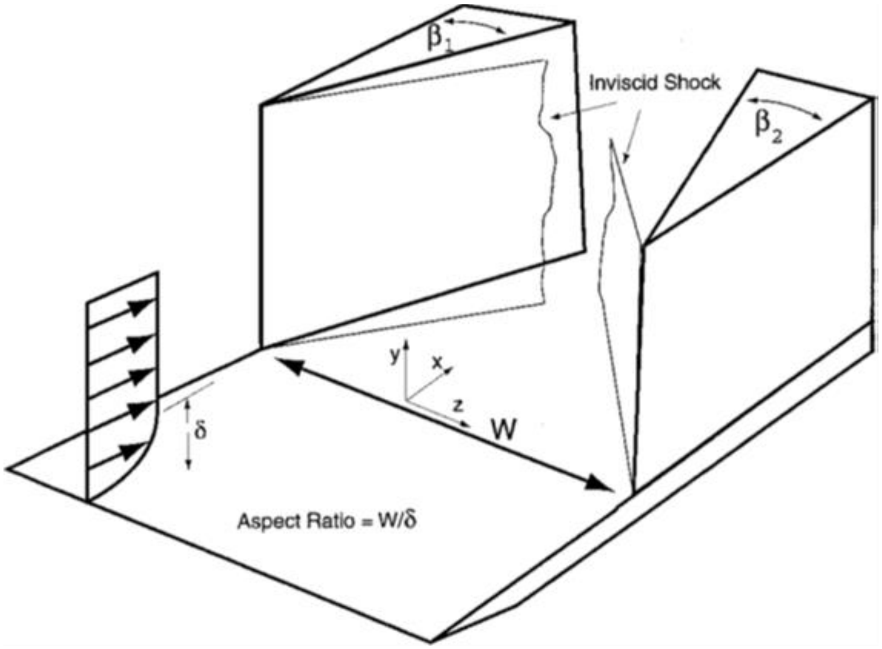

Figure 2.1. Crossing shock-wave/boundary layer interaction. [30]

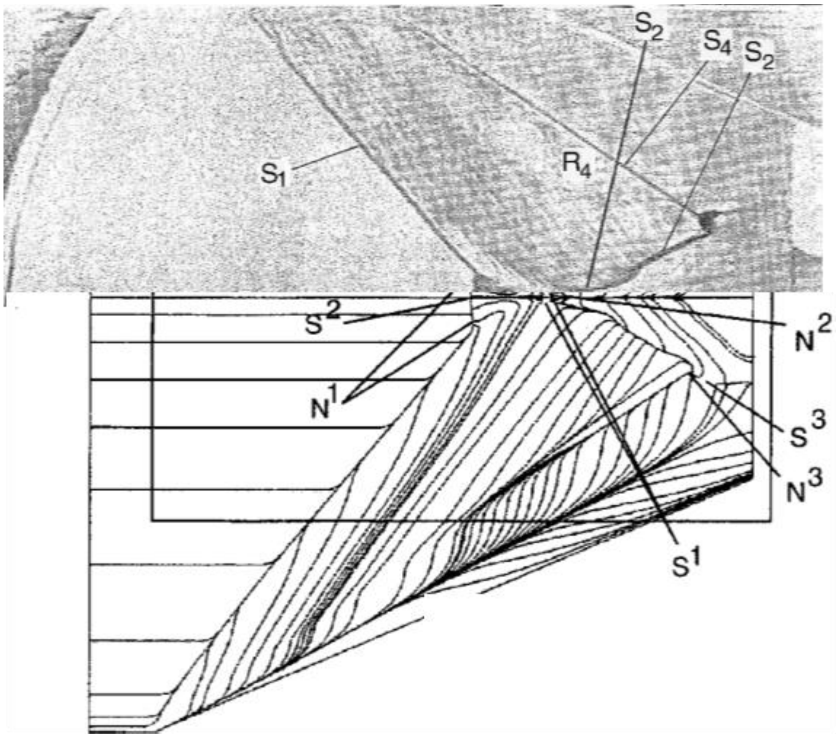

Figure 2.2. Comparison of experimental oil flow and computational stream lines which show good agreement [30]

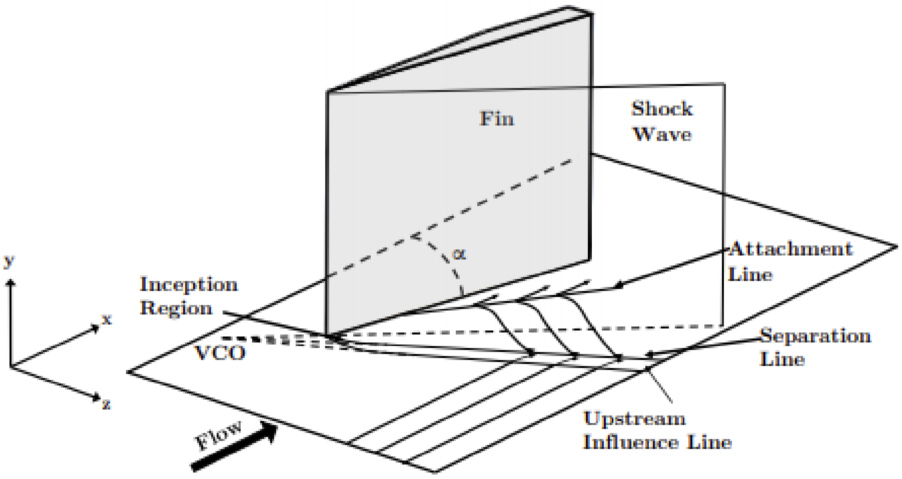

Figure 2.3 Footprint of the swept shock interaction. [34]

Vortex Generators

Due to the potential negative impacts of SBLI on the flow field, various methods of control have been studied in relation to SBLI [35] [36] [37] [16]. Control of SBLI is important for increasing efficiency of these vehicles and is used to increase inlet efficiency [16] [11] [37]. Inlet performance is typically characterized by total pressure recovery and flow distortion [18]. Various methods of passively controlling flow have been studied in relation to SBLI in inlets to reduce the loads on the vehicle and to prevent unstart [36] [38] [27]. Passive systems, such as vortex generators, are ideal as they are simpler to employ, add less weight to the vehicle, and are robust compared to active flow control systems, such as bleed or suction systems [39]. Vortex generators (VGs) provide a reduction in flow separation [39], but also are additional intrusions into the flow. The flow around a VG in supersonic flows is still an area of research and has not been studied as extensively as for subsonic flow [39]. The VGs produce changes in the boundary layer which improve its ability to manage with adverse pressure gradients. They achieve this by taking energy from the freestream and redistributing it into the boundary layer through two horseshoe vortices [39]. Reducing the VGs to sub-boundary layer heights and placing them closer to the interaction minimizes their impact on the flow field while still reducing separation [39].

However, the ideal arrangement of the VGs, as well as optimized size, is dependent on other factors. Ramped vanes have been shown to be a highly effective VG shape and their height is a major factor in their effectiveness [40]. Studies have been done experimentally to study VGs in high speed flows, such as McCormick who showed that sub-boundary layer VGs suppress SBLI in low Mach number cavity flows [40] and Barter and Dolling [36] [41] who showed that VGs improve boundary layer characteristics to minimize pressure loads caused by SBLI in a Mach 5 flow. While the VGs do show a reduced separation region, there are still major questions as to how they affect the bulk flow characteristics of pressure recovery, unsteadiness, and drag [39]. One of the limits with introducing VGs remain in an increase in corner flow effects and 3-dimensionality of the SBLI [39] [42]. There have been few studies of using VGs in inlet type flow paths [39] and this is an area this work seeks to address.

Many CFD studies only have a single vortex generator due to difficulty resolving the flow around such a small protuberance. Thus, many studies focus more on the localized impact of the VGs compared to the bulk flow field effects. The localized impact of a VG can be seen in Figure 2.4. Experimental studies typically include an array of VGs [39]. As more vortex generators are introduced in computational studies, experimental validation is needed. Additionally, these studies can optimize the variation available with CFD to study a variety of VG types and configurations with the validation of a few key data points experimentally.

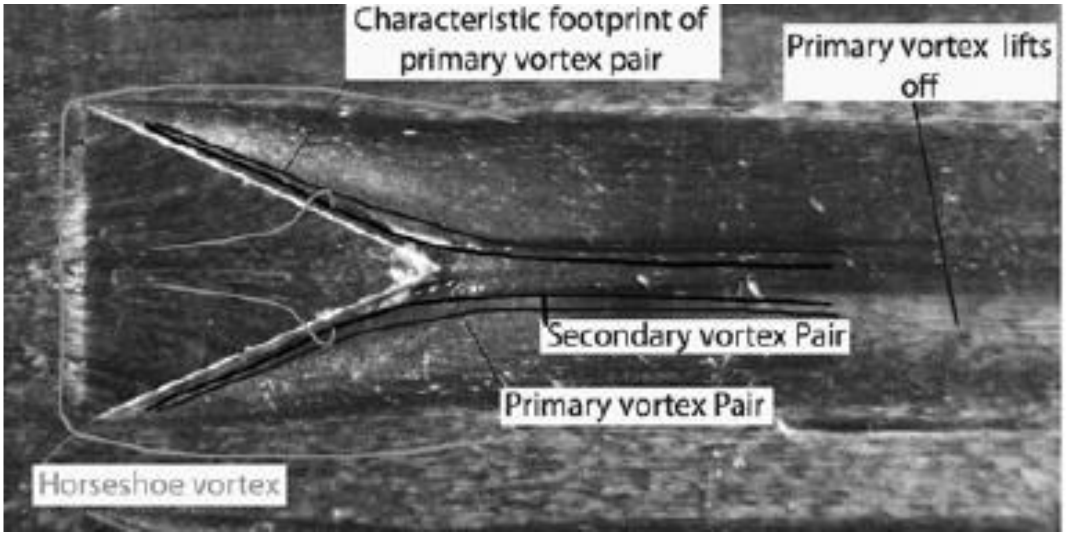

Figure 2.4. Localized flow effects of a vortex generator [38]

The goals of this research are to provide validation for CFD research into the effectiveness of vortex generators on a crossing shock-wave/boundary-layer interaction generated by a double fin configuration as seen in Figure 1.3 VG number and configuration were investigated and the best arrangements were determined experimentally and will inform the computational study. This combines the accuracy of experimental studies with the variability of computational studies. The separation location is determined and used for quantitative analysis and comparison with the CFD results. However, unsteady results have been identified as a point for future validation of unsteady CFD on VGs as applied to SBLIs [39] [42].

Figure 2.5 shows the optimization of vortex generator size that was used in this study. In addition to the dimensions shown, h was 40% of the boundary layer height to minimize total pressure loss and prevent additional SBLIs caused the VG. In a supersonic flow, any flow blockage will cause a shock to be introduced. To minimize this, the VGs are only 40% of the boundary layer height which has been determined to balance between the flow changes of the VG and the shock impact in the flow [43]. The dimensions of the VGs were then scaled via the findings of Lee et al. that suggest a micro ramp VG shape with the dimensions based on the height (h) chosen. The length of the VGs is $6.57h$ and the width is $5.48h$ [43]. These locations were determined due to studies done by Lee et al [44]. The ideal configuration in this study was to place the VGs 15δ upstream of the interaction and $8.36h$ apart [44]. Further discussion of the model design and choices can be seen in the Experimental Methods section.

Experimental Set Up and Diagnostics

Fins and Vortex Generator Model

The models tested were two symmetrical fins that are 114.3 mm (4.5 in.) tall and 194.8 mm (7.67 in.) long with a leading angle of 10 degrees. They were made of aluminum and attached to the tunnel sidewall. The double fin geometry created a crossing shock-wave/ turbulent boundary-layer interaction interacting with the fully turbulent boundary layer on the test section floor of the tunnel. The double fin geometry can be seen in Figure 2.1 [30]. Vortex generators were placed in front of the fins for flow control. The vortex generators were 3D printed and made of ABS plastic which were adhered to the tunnel test section floor via adhesive. A general schematic of the vortex generators in relation to the fins can be seen in Figure 2.6. The single VG cases only had the center VG present. The 3 VG cases all had three VGs, but at varying locations in front of the fins. However, due to the location of the nozzle in the Mach 2 facility and the 8 in. by 8 in. test section these dimensions were held as close as possible, but small modifications to the VG locations were made. The maximum distance upstream from the separation line of the baseline case was 4.75 inches and the VGs were 4 inches apart.

Figure 2.5. Optimized dimensions of a VG in supersonic flow [43]

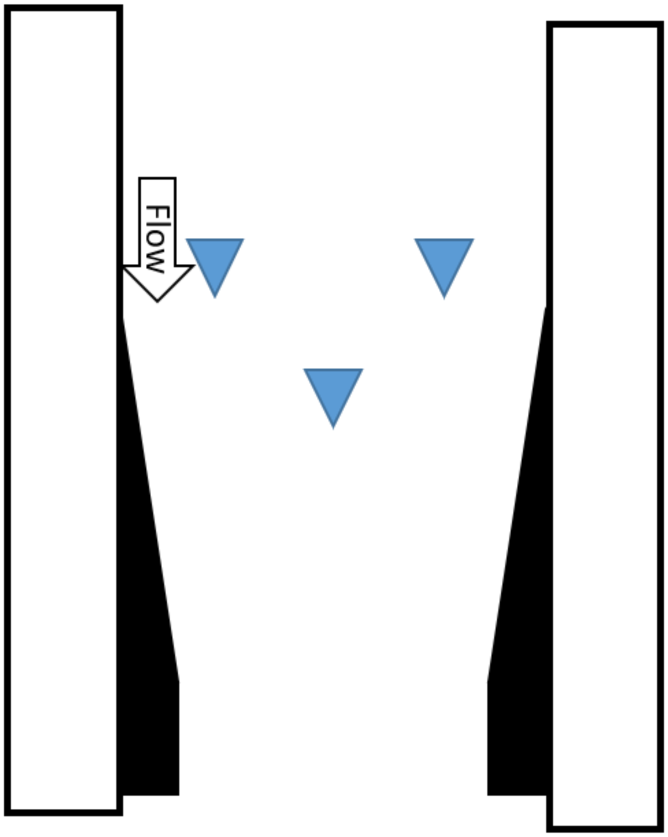

Figure 2.6. Representative model schematic.

The test matrix of runs shown in this paper is shown in the following Table 2.1. Test Matrix of Vortex Generator Configurations. The main difference between the main three configurations is the distance from the leading edge of the fin to the leading edge of the vortex generator. The maximum distance case was based on the literature as already discussed, but due to limitation of the test section the vortex generators were placed as close to the nozzle as possible within geometry constraints of the tunnel. The remaining two cases were each moved an inch further downstream respectively from the maximum case. They are referenced by the distance from the leading edge of the VG to the separation line of the baseline case. This flow feature is further discussed in the Results section of this chapter.

Surface Oil Flow Visualization Experimental Setup

Oil flow shows the mean flow topology for an interaction and has been used frequently in the literature to define SBLI features [33]. Surface oil flow visualization was used to provide a visualization of the mean flow via surface streamline patterns. Approximatley, 1,000 images were acquired with the Photron FASTCAM MINI AX200 at a frame rate of 50 Hz and a resolution of 1,024 × 1,024 pixels. The camera was mounted above the test section floor in order to image the transverse plane of the flow. Rocket red dye was mixed with mineral oil in a 1:3 ratio by volume, applied to the surface of the plate in the entire field of view, and illuminated by black lights. The oil traced the mean flow structure during the run and was recorded via the camera. Then, a single representative image was chosen for analysis.

Pressure Transducers

Static pressure ports in the stagnation chamber and downstream of the model were used to determine total pressure recovery and compare to the CFD results. The pressure transmitters were Rosemount 1151DP which have a reference accuracy of ±0.075% [45]. Figure 2.8 shows where the pressure ports are located along the floor of the wind tunnel. The large gap between the first port and the second is due to the floor insert used to mount models in the tunnel. The pressure transducers acquire at 100 Hz.

Results

The results for CSWBLI experiments are shown in the following sub-section. The results are primarily of the oil flow data, as it shows the effectiveness of the VGs at moving the separation location downstream. The results of different arrangements are shown as well. This was one of the major research questions of the study: how effective are VGs at changing separation location and in what arrangement? The pressure data was mainly used as a quick check between the computational results and the experimental results in the beginning, but it is shown as well. Additionally, the comparison data between the experimental and computational work is shown as it was also one of the main goals of the experiment: to provide validation data for the simulations.

Table 2.1. Test Matrix of Vortex Generator Configurations

Run #	**Configuration**	**VG#**
8	Baseline Case	0
4	x_s= 4.75 (angled)	1
5	x_s= 4.75	1
6	x_s= 4.75	3
9	x_s= 3.75	3
11	x_s= 2.75	3

Figure 2.7. Oil mixture painted on the test section floor and illuminated by black light before a wind tunnel run.

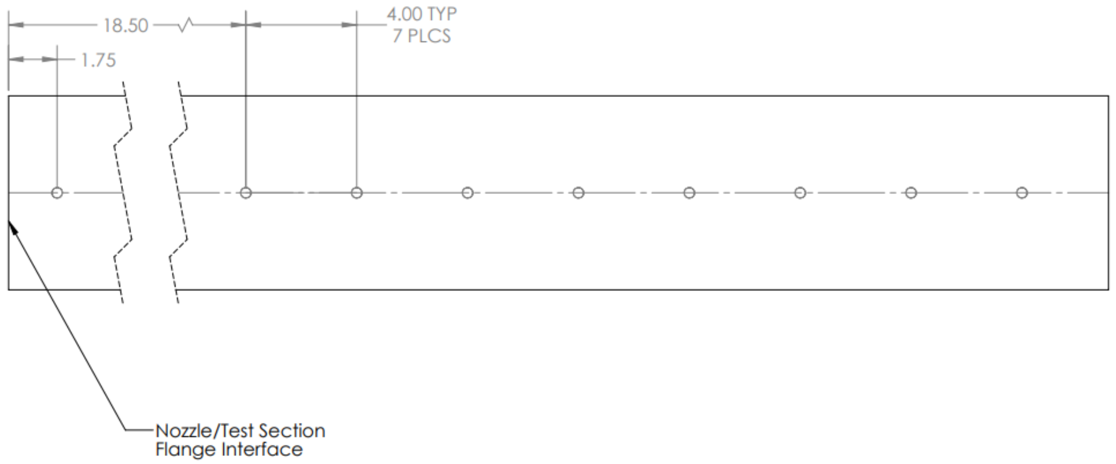

Figure 2.8. Pressure transducer locations along the wind tunnel floor.

Oil Flow Results

The results of the oil flow experiments are shown below in Figure 2.9. Oil flow images show the mean flow of the interaction and the effect of the vortex generators on the interaction. These images were given a false color map in ImageJ [46], an image processing software. All images seen of the oil flow, unless otherwise noted have the same color map applied. This allows the flow features to be more easily seen and measured. The images show the mean streamlines and separation location in the lighter colored regions, which corresponds to the oil locations. The CSWBLI is a symmetrical interaction [3] and thus, the images shown below are all cropped to show one side of the interaction. This allowed the pixel resolution to be greater in the areas of interest. Figure 2.9 shows the oil flow results from the different vortex generator cases. It is difficult to determine the difference in separation location only visually, thus a quantitative measurement was needed as well.

While the oil flow in Figure 2.9 is qualitative, determination of the separation distance provides quantitative insight. The separation location was determined by finding the intersection of the line of separation with a line drawn along the point where the shocks cross and the flow oil turns parallel to the tunnel sidewalls. An example of these lines and their intersection for the baseline case can be seen below in Figure 2.10. This intersection was determined to be the separation location and agreed with the separation scale obtained from computational skin-friction and streamlines determined in the computational portion of the work.

ImageJ [46] was used for the image processing and resulted in an error of approximately ±4 pixels resulting in ±0.03 inches for this analysis. Figure 2.11 shows the separation distance measured from the leading edge of the fin for all the cases referenced with error bars for the aforementioned errors. The separation distance is normalized by the boundary layer height measured at 11 mm measured by Kocher et al. for the Mach 2 facility [16]. The quantitative analysis shows the effect of the vortex generators on separation location. This delay of separation shows that the vortex generators are performing effectively for this metric of performance, which suggests that VGs would be an appropriate tool to delay separation in inlet type geometries.

Figure 2.11 shows that the optimized vortex generator configuration was the x_s = 3.75 in. case, as it delays separation to the furthest downstream location. The x_s = 4.75 case is relatively similar to the baseline case, and the x_s = 2.75 in. case is the worst case at delaying separation. This shows that there is a limit in effectiveness as the VGs get closer to the interaction. Also, in Figure 2.9, the x_s = 2.75 in. case can be seen to have some interaction with the floor inset junction that the VGs are very close too. The VGs were also placed nearly on top of the original separation line of the baseline case. This could also contribute to the significant decrease in separation distance compared to the other cases.

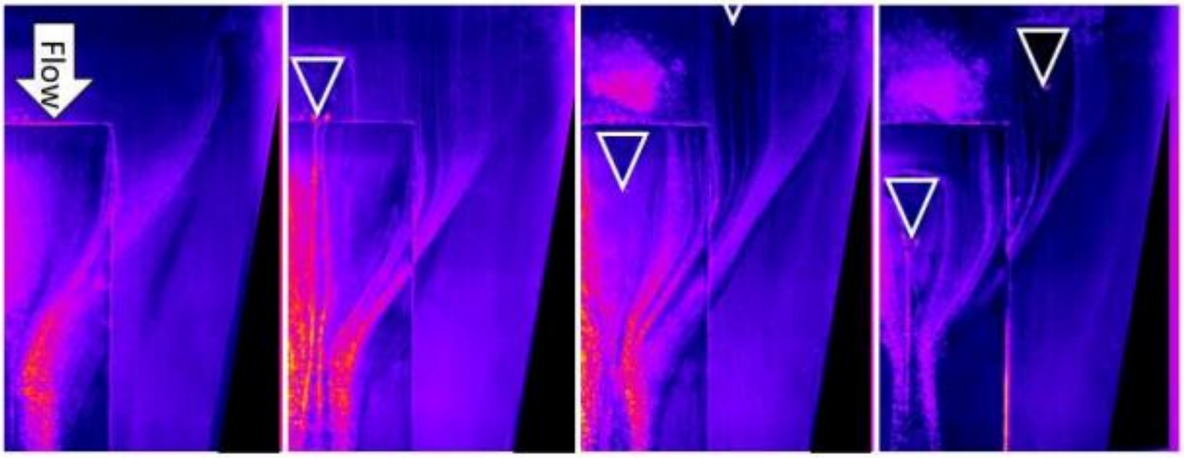

a) Baseline Case **b) x_s=4.75 Case** **c) x_s=3.75 Case** **d) x_s=2.75 Case**

Figure 2.9. Case comparison between the baseline and all three VG cases.

Figure 2.10. Example of how separation distance was determined for the baseline case.

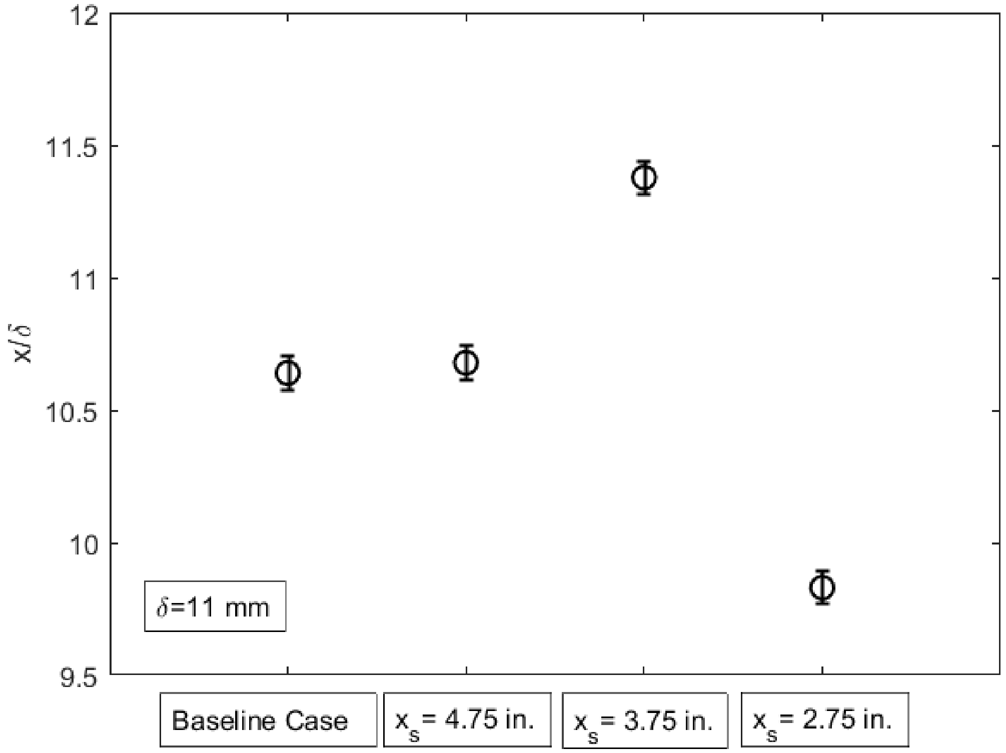

Figure 2.11. Separation distance from the leading edge of the fin normalized by the boundary layer height.

Additionally, cases were run with a single VG. The results showed that the 3 VG configurations were much more successful at moving separation downstream. The results of these two cases are shown in Figure 2.12, which shows the difference between the two cases with only 1 VG at the centerline. In image a), the VG was not placed perpendicular to the flow. This caused non-symmetrical effects with the shock structure. While the VG was only placed a few degrees off perpendicular, this shows that the placement of the VGs is critical to their performance in inlet like flow paths. The off-center case did have a reduction in separation distance compared to the baseline case and the single x_s=4.75 case. However, there was not much of a difference in the single VG cases compared to the baseline case.

This interaction has the typical conical flow features associated with a fin generated interaction [33] discussed previously, which can be seen in Figure 2.13. The conical structure of the interaction is represented by the upstream influence line, the separation line, and reattachment line. These all converge at the virtual conical origin which is upstream of the fin leading edge. The fin generates a planar oblique shock, and the features have quasi-conical symmetry in planes normal to the shock. Additionally, the quasi-conical nature of the interaction does breakdown at the shock-shock interaction in the region of separation. Another way to investigate the performance of the VGs was to compare the angles of the major flow features of the interaction. These flow features are labeled in Figure 2.13.

Again, quantitative measurements can be extracted from the oil flow images. The angles of these features as measured from the tunnel sidewall are compared in Table 2.3. It can be seen that the angles decrease for the optimized VG case for the separation and reattachment angles. This also suggests that separation has been moved further downstream. However, the upstream influence angle increased in comparison to the baseline case. The VGs were very close to the upstream influence region and thus they may have contributed to that area turning earlier. Thus, the separation and reattachment regions confirm the results concluded from the separation location analysis. This shows that the VGs are changing the initial shock structure as well as the separation region. The error for these measurements is ± 1° as measured in ImageJ [46]. These angles were measured based on the region of the flow closest to the tunnel centerline. Thus, the impact of the sidewall boundary layer could be excluded from the results.

In addition to the oil flow data, static pressure measurements were taken along the tunnel centerline. Figure 2.14 shows the pressure values for the various run conditions before the interaction in the undisturbed flow and after the interaction where the pressure has recovered. These measurements were primarily used as a quick check with the initial CFD cases to match conditions and confirm initial results.

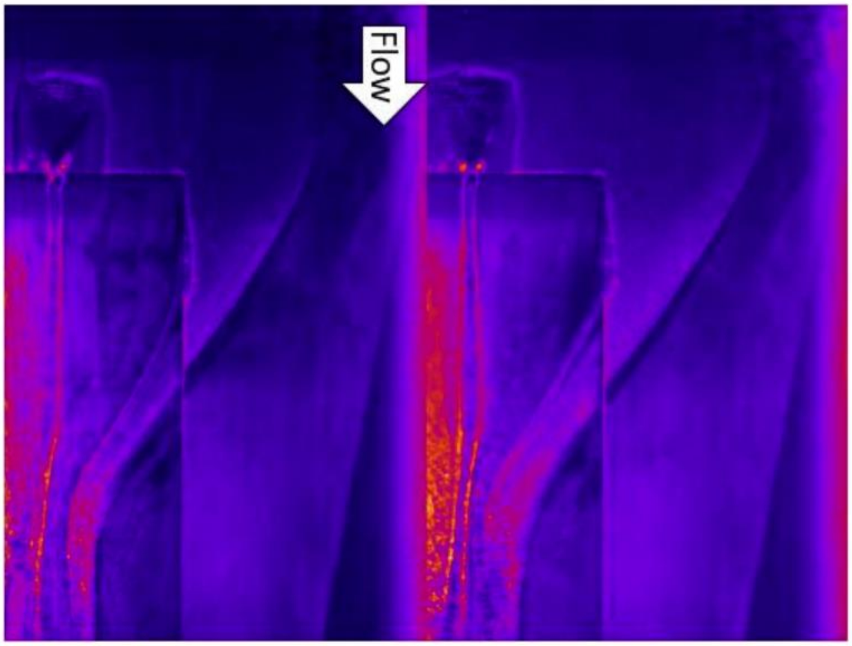

a) Single VG Case b) Single Misaligned VG Case

Figure 2.12. Single VG Cases.

Table 2.2. Results of single VG cases compared to baseline.

Case	**x/δ**
Baseline	10.64
x_s=4.75 in. single	10.65
x_s=4.75 in. single mis-aligned	10.56

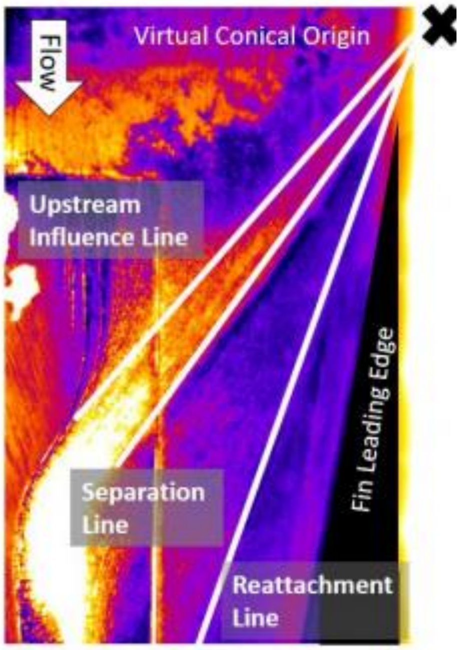

Figure 2.13. Flow features of the conical structure interaction for the baseline case.

Table 2.3. Comparison of quasi-conical structure between baseline and optimized VG cases.

Flow Feature	**Baseline Case (°)**	**Optimized Case (°)**
Upstream Influence	45.5	47.3
Separation	36.4	32.1
Reattachment	18.5	16.4

CFD Comparison

One of the main goals of this research was to use the experimental results to refine computational studies. The first step in this process is to compare the CFD simulations to those already shown in the experimental results. The computational results were done by Schwartz et al. and additional details about the computational process can be seen in the AIAA conference paper "Passive Flow Control on a Crossing Shock-Wave/Boundary-Layer Interaction. [22]" RANS simulations were preformed with the HPCMP CREATETM-AV Kestrel flow solver component Kestrel CFD solver (KCFD). These simulations model the bulk, mean flow. Since oil flow also shows mean features, comparing the two analysis tools is an effective comparison. In Figure 2.15, the separation locations from the experimental data are shown in comparison to the computational results of Schwartz [20]. This is the same experimental data presented in Figure 2.11. The computational results are well within the margin of error for the experimental data of ±4 pixels. The difference in the results is quantified in Table 2.4 by calculating the percent difference between the experimental and computational separation points. The separation points for the computational data were taken with the same methodology as the experimental results in addition to looking at the skin friction coefficient, where the negative value for skin friction is a separation location.

In addition to the quantitative comparison, a qualitative comparison can be made between the oil flow images captured and the numerical streamlines computed. As seen in Figure 2.16, the oil flow on the top of the image (with the color map removed) mirrors well with the CFD streamlines for the baseline case. The second image shows the oil flow overlaid with transparency on the numerical streamlines, which also shows good agreement. Matching the baseline cases was the first step in understanding if the code could accurately reproduce the experimental results. As this was the first time Kestrel was used to model internal flows, matching the baseline case was an essential first step in proving the validity of the computations.

The other main question of the study, after the experiments showed that the vortex generators were effective in moving separation downstream, was if the CFD simulations can model the effects of the vortex generators in the mean flow field. Thus, the VGs were added to the simulations in the optimized arrangement and compared to the optimized experimental result. As seen in Figure 2.17, the vortex generators are seen in orange in the CFD section of the images. In these images, the VG alignment between CFD and experiment is not perfect as CFD places the vortex generator exactly 2 in. from the sidewall and in the experiment that distance was measured and placed by hand. Even with this discrepancy, the images show good qualitative agreement.

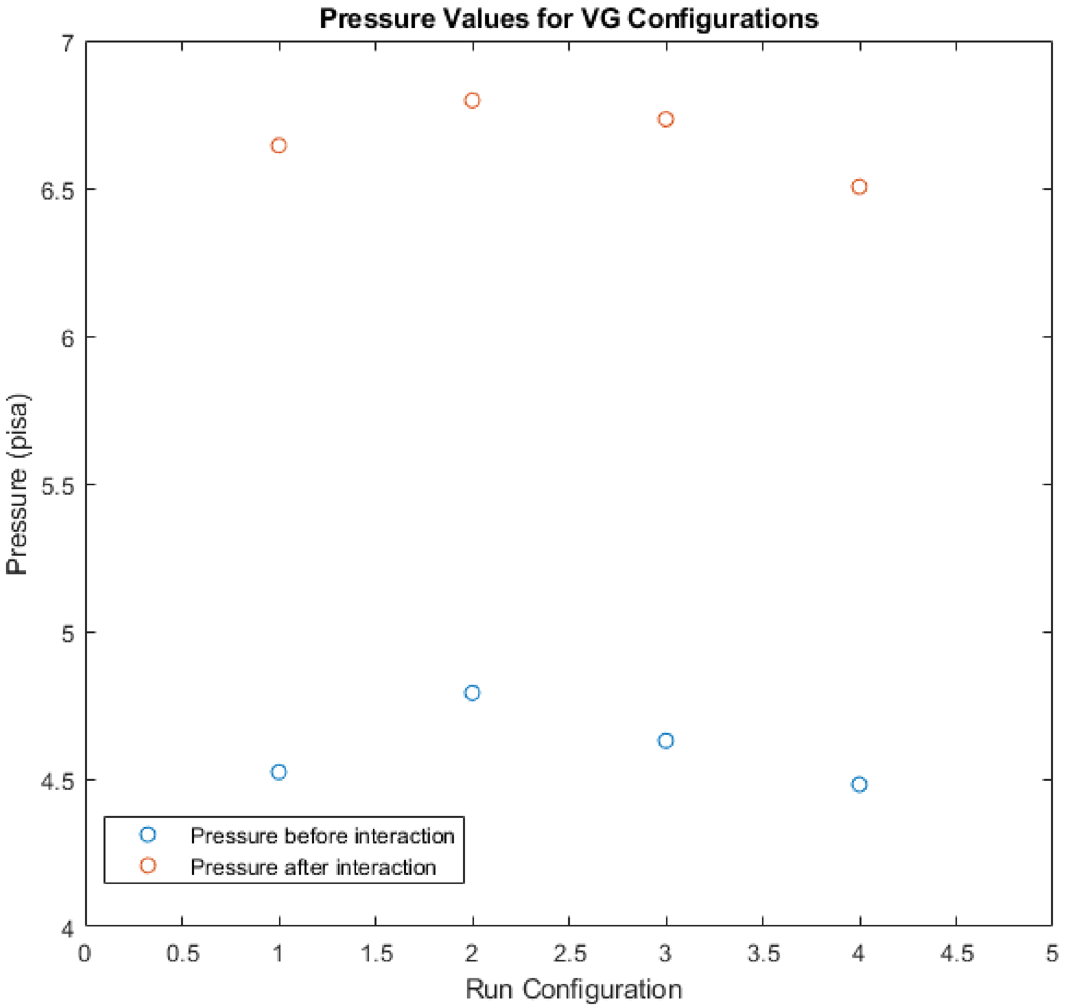

Figure 2.14. Pressure values for the different VG configurations both before and after the interaction.

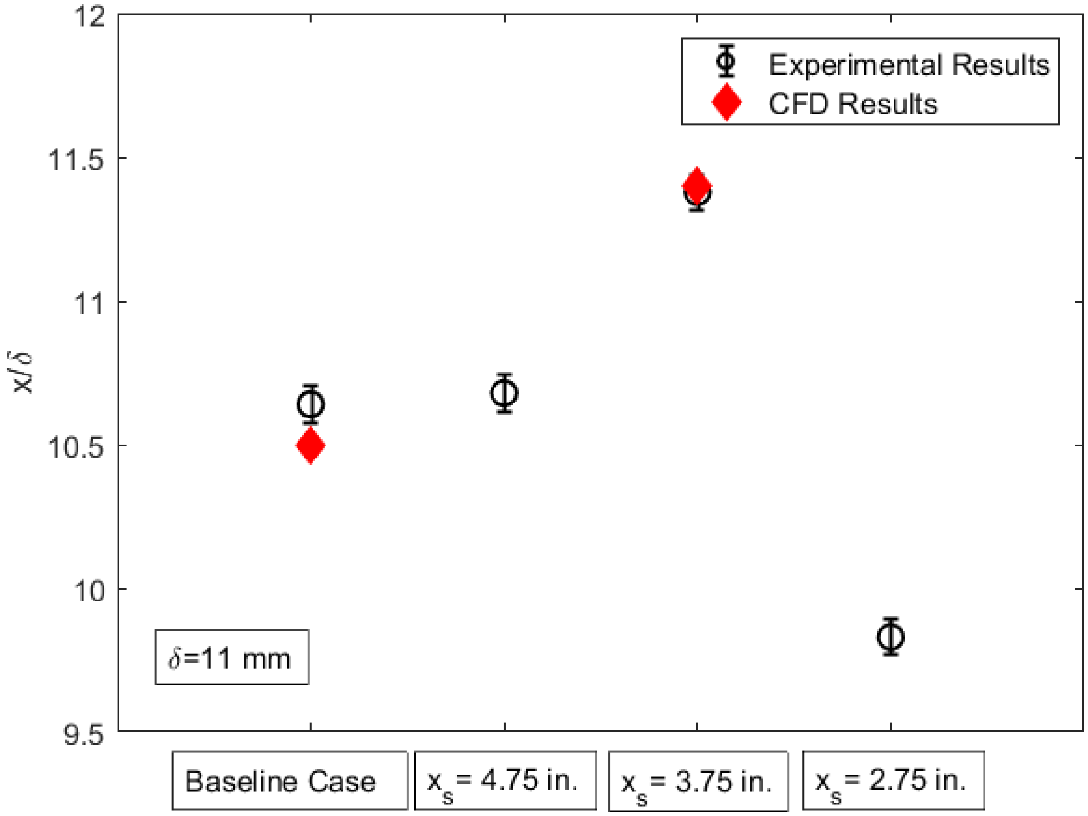

Figure 2.15. Comparison of separation data for the experimental and CFD cases. CFD results from Ref. [20] and Ref. [22].

Table 2.4 Percent difference between the computational and experimental separation distance.

Case	**Percent Difference**
Baseline Case	1.3 %
Optimized VG Case	0.3%

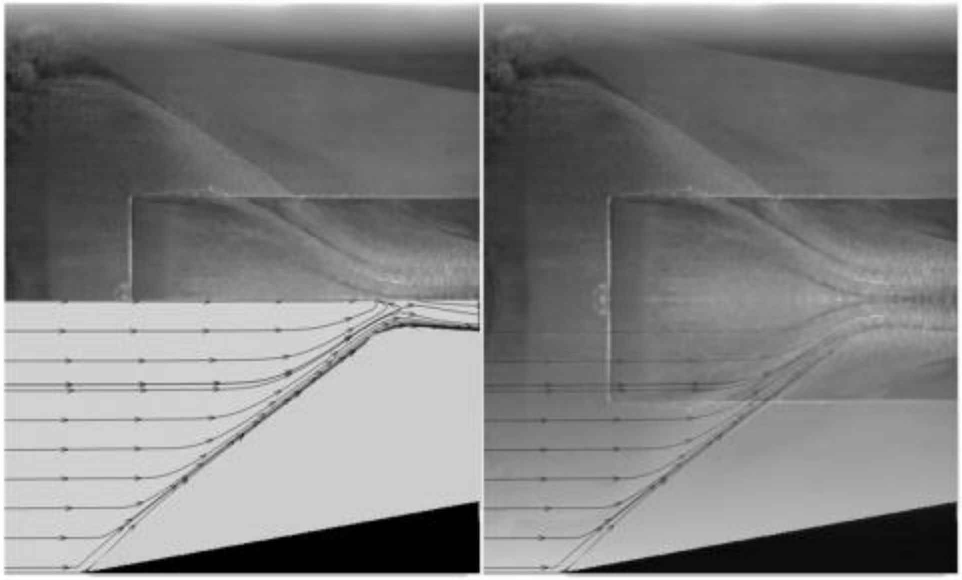

a) Side by side comparison b) Oil flow overlay on CFD streamlines

Figure 2.16. Experimental oil flow compared with computational streamlines for the baseline case. Flow is left to right. Simulations are from Ref. [20]

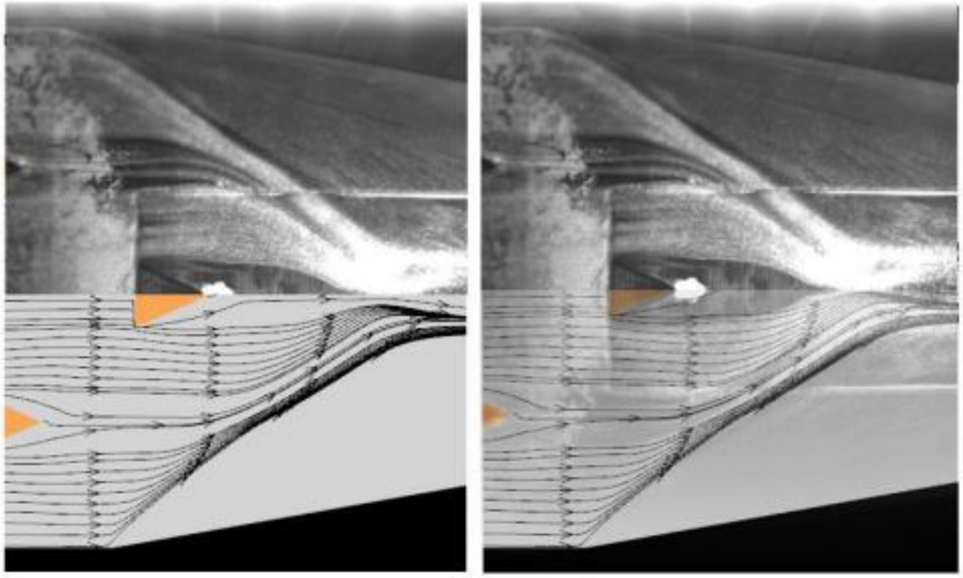

a) Side by side comparison b) Oil flow overlay on CFD streamlines

Figure 2.17. Experimental oil flow against computational streamlines for the VG case. Flow is left to right. [20]

After the simulations were shown to match the separation location of the baseline case and the optimized VG case, the computations can reliably be used to examine additional parameters of the mean flow field such as total pressure recovery, distortion, and momentum losses. These can be extracted from the CFD results for additional analysis. As VGs have primarily been investigated in localized experiments, their impact on global flow field properties was investigated in this experiment. As the experiments did not measure bulk flow field parameters, the simulations provided this analysis. As seen in Figure 2.18, the vortex generators do have a negative effect on the stagnation pressure recovery, a vital indicator of inlet performance. The lower pressure area on the floor is increased due to the protuberance of the VGs. This image is looking into the flow of the wind tunnel in the spanwise and wall normal directions, which is a different plane than the images shown previously and was extracted 8δ downstream of the end of the fin. The bulk flow analysis is an example of the additional data that can be acquired using CFD which is difficult to measure experimentally.

Impact of the Sidewall Boundary Layer

One of the main differences in this experiment compared to those seen in the literature is that the fins are mounted to the sidewall of the wind tunnel rather than in the freestream. Single sharp fin interactions have traditionally been done with clean flow [32] [33] [30]. The sidewall has a sidewall boundary layer in which the fin is placed, rather than just the freestream flow. This introduced the question of how much of an impact does the sidewall boundary layer have on the interaction?

Figure 2.19 shows a single fin generated interaction made by removing one of the symmetrical fins in the experimental set up detailed in Figure 2.6. Then, in the same UTSI Mach 2 facility, a single fin interaction was generated at the tunnel centerline at a 10° angle of attack. This interaction was captured with oil flow as well and is seen in Figure 2.20. A third comparison is made to a case from the literature with the work done by Arora et al. [33] This is another case of a fin generated interaction at a 10° angle of attack in a Mach 2 flow, but at a higher Reynolds number of 47×10^6 m^{-1}. This interaction was visualized using oil flow was well and can be seen in Figure 2.21.

The differences this causes to the interaction are characterized below in Table 2.5, where α_{fin} is the fin angle of attack and α_i is the Korkegi criterion, which determines what angle a shock generator must be at for a turbulent SBLI to have separated flow [47]. All the fins in this study meet the requirements of the Korkegi criterion. The angles were measured by the same methodology used earlier for the conical approximation of the CSWBLI.

From these results, the sidewall boundary layer does have an impact on the fin interaction. The angles for the shock structure are lower, which suggests the sidewall boundary layer moves the interaction and its separation point downstream. The two features are still only about 3-4° difference for all the fin cases, so moving one to a lower angle will move the other as well. Potentially, this could be used to move the separation point downstream without the protuberances caused by the VGs. This is likely a result of the boundary layer causing an increase in the viscous area of the SBLI. The flow has a delayed separation region as the flow needs less energy to recover to inviscid structures. However, it would likely need further study to fully characterize the flow changes and other potential adverse effects.

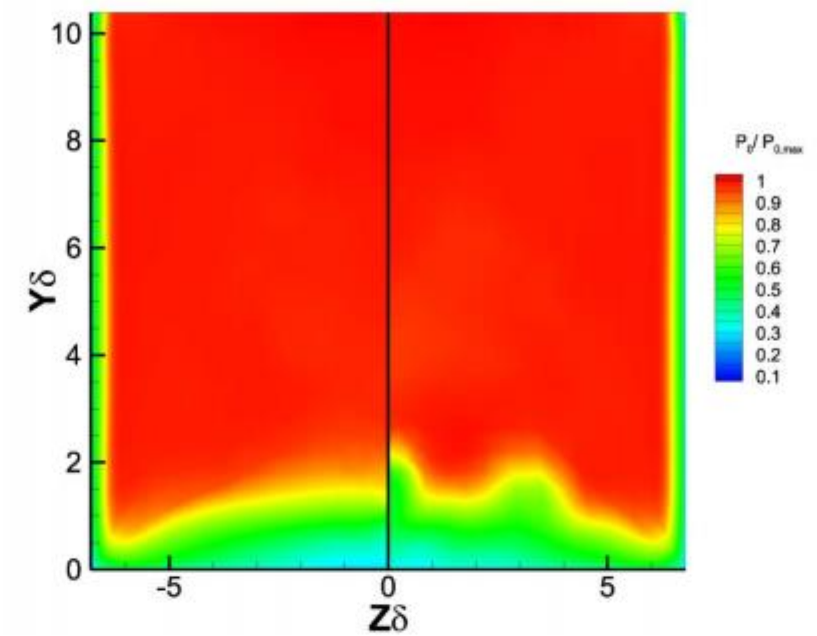

Figure 2.18. Outlet stagnation pressures without VGs (left) and with VGs (right). Flow is into the page. From Ref. [20]

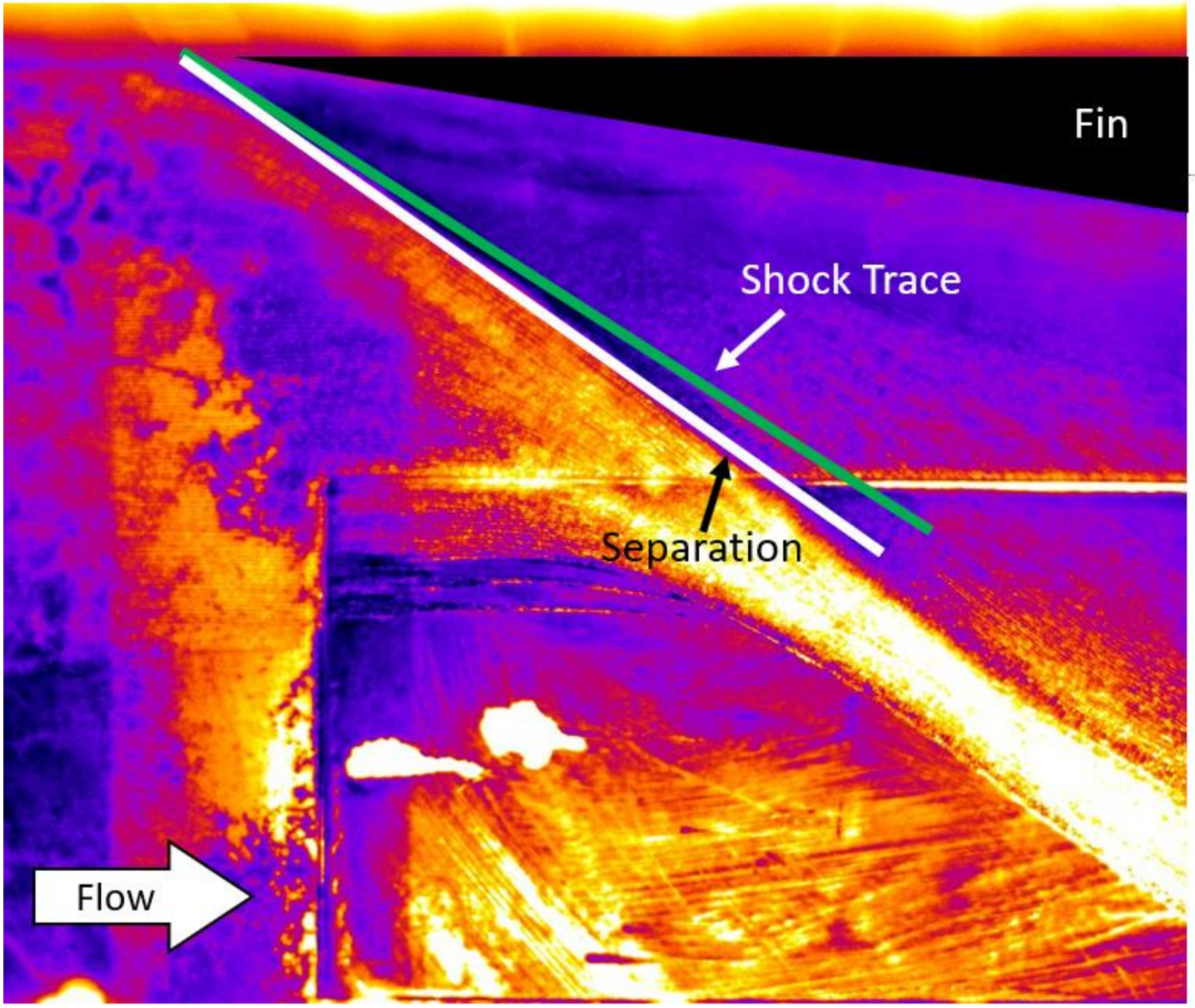

Figure 2.19. Oil flow image with false color of single fin SBLI with the influence of the sidewall boundary layer.

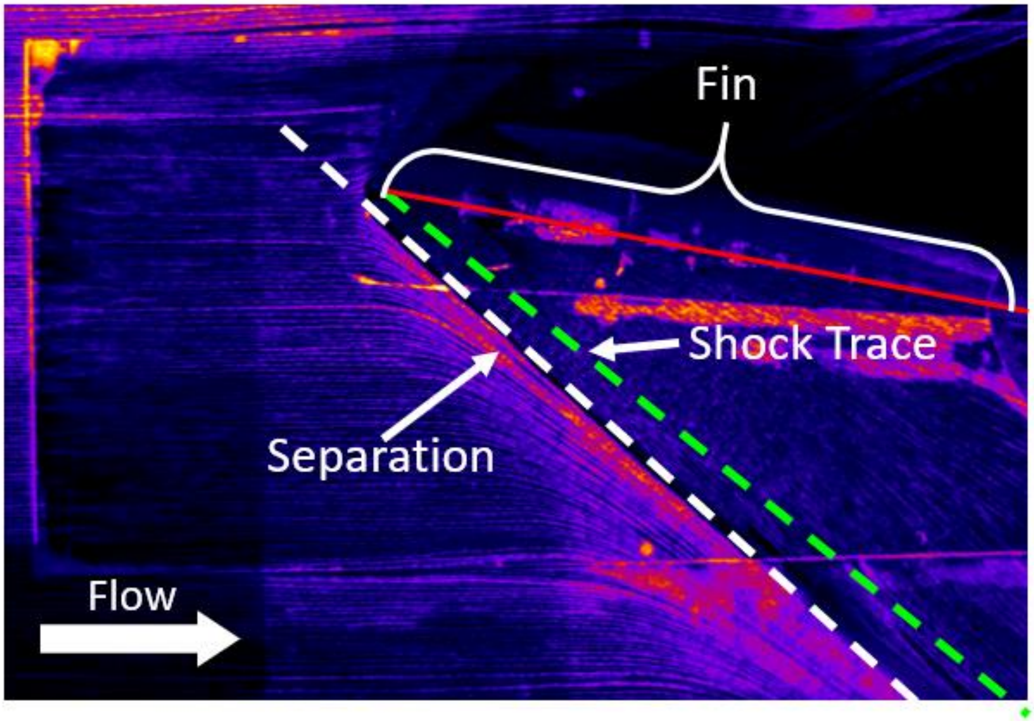

Figure 2.20. Oil flow of fin at 10° angle of attack in the UTSI Mach 2 wind tunnel. *Courtesy of Douthitt et al.*

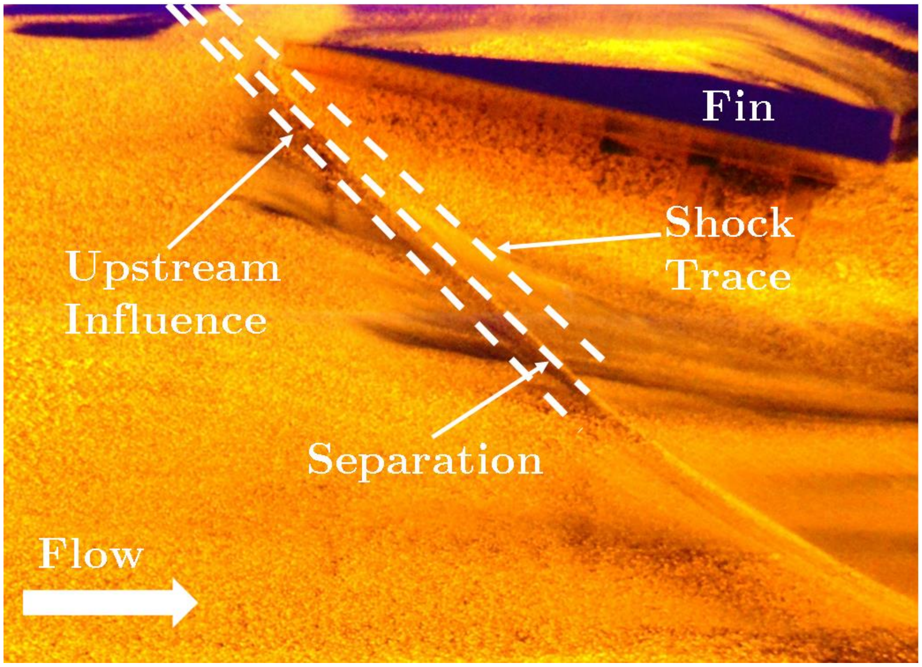

Figure 2.21. Fin generated SBLI at 10°. [33]

Table 2.5. Comparison of fin generated SBLI quasi-conical structure

Case	**α_{fin} (°)**	**α_i (°)**	**Shock trace (°)**	**Separation Line (°)**
Sidewall Fin	10	8.6	33	37
UTSI fin	10	8.6	39	42
Arora Fin [33]	10	8.6	39	43

Uncertainty Analysis

The uncertainty in these measurements is primarily conveyed in the results through the error bars in Figure 2.11. These values were measured via ImageJ [46], a image processing tool used in many scientific analyses as it was created to prioritize quantification and measurement over image editing [48]. The error is ±4 pixels resulting in ±0.03 inches for the separation location measurements. This was determined as the separation location was found as the intersection of two oil flow line traces. This resulted in error that can propagate from the line trace as well as the intersection point. Thus the ±4 pixels error approximation was chosen as a conservative estimate of the error in these measurements. While the oil can be seen in some regions to have some discontinuities or pooling, this is due to an excess of oil gathering in the interfaces between the wind tunnel floor and the inserts. Later in the run, the oil would be blown downstream causing pooling effects. This did not interfere with the results of the oil flow.

For the angle measurements of the quasi-conical structure in Table 2.3 and Table 2.5, the uncertainty is ±1° as determined by multiple measurements of the angles. The repeatability when focused on the flow closer to the centerline of the tunnel provided greater accuracy. The error of the pressure measurements was ±0.075% [45].

Additional sources of error in this experiment could result from improper VG placement. As Table 2.2 showed for the misaligned single VG, there can be negative effects of VG placement. As shown for subsonic flows, there is a benefit of having a large number of VGs. However, as the VGs were scaled based on the boundary layer height. A maximum of three could be placed in the wind tunnel with the suggested distance in between them as recommended by the literature [44].Thus, a study with a larger amount of VGs, either due to a smaller boundary layer height or larger wind tunnel test section size could investigate the benefits of a lager array of VGs.

More information on the uncertainties in the computational work done by Schwartz et al. and presented here can be seen in Ref. [20] and Ref. [22].

CHAPTER THREE

UNSTART EXPERIMENT

If at first you do not succeed, try two more times so that your failure is statistically significant.

This work was supported under CFDRC project number 9326.

Literature Review

As mentioned in the Introduction, unstart is a process that is typically studied by looking into the isolator section of the scramjet flow path. Unstart remains one of the major problems for scramjet engine design.

The Unstart Problem

Unstart is generally defined as the breakdown of supersonic flow. This term is typically used in relation to high speed air breathing vehicles and other engines. For these engines, unstart means that the necessary supersonic flow for the engine to operate has broken down in some way. Unstart causes a significant loss of engine performance or structural damage. An unstart event in a scramjet is generally considered a loss of the vehicle [18].

For the SR 71, the world record holder for fastest aircraft, the ramjet engine had a notorious problem with unstarting midflight. An unstarted versus started inlet can be seen in Figure 3.1. The unstarted inlet has ejected the shock train and a bow shock forms outside of the engine. As this engine was a ramjet with other things, an unstart event meant the pilot might bang their head against the side of the cockpit, but the vehicle could recover [10]. For scramjet flow paths, the margin of error is much smaller due to the need for supersonic flow [18].

Unstart relates back to basic compressible flow principles of the area to velocity relation [23]. If the subsonic region of the shock train creates enough blockage that supersonic flow can no longer pass, then essentially a second throat is created and the engine unstarts. For engines, there are several possible causes of unstart and due to the highly linked nature of scramjet engines it can be difficult to determine which processes are causes or effects [19].

As mentioned above, unstart is still an area of great research interest with many fundamental questions still unanswered. In the literature, there is still no consistent definition or declarative onset metric. Many have been proposed and studies such as: shock position/speed, separation region location of the leading shock, shock train length as a function of pressure in time or the axial direction, Mach stem height, and corner separation [19]. CFD simulations have been primarily RANS studies with some higher fidelity models [19] [49], but a limited analysis on the uncertainties of these models and the experimental data has been performed [19]. With so many of the fundamentals still in question, the uncertainty in these studies is great. Scramjets are so complex that it is extremely difficult to test a full vehicle in ground testing. Thus, computational studies must be relied upon as well. For these studies, a greater understanding of the uncertainty is necessary to make better decisions in flight vehicle designs [19].

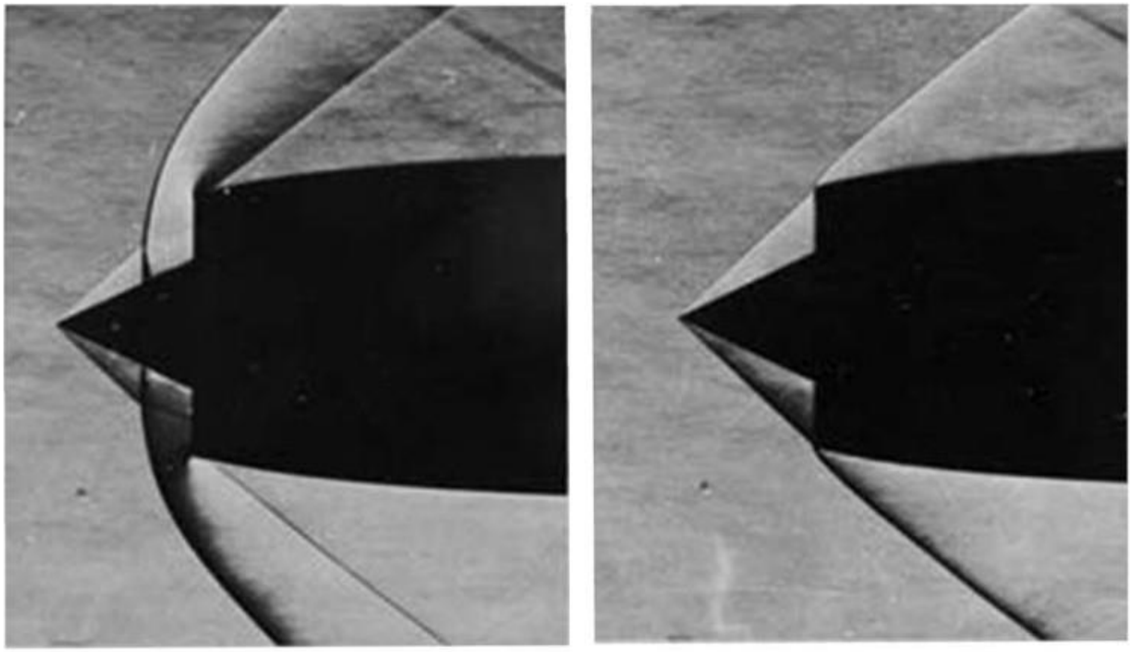

Unstarted inlet

Started Inlet

Figure 3.1. Inlet of a SR 71 in unstarted and started conditions. [50]

Additionally, sometimes when the shock train is not fully ejected from the flow path, the shock can oscillate at high frequencies in one location, known as buzz. This oscillation, much like that of SBLIs, can cause structural damage to the vehicle from the high acoustic and pressure loads. An example of the types of pressure loads that can be caused by “buzz” can be seen below in Figure 3.2 [51].

Start and unstart can also be used to describe the process of bringing a wind tunnel up to condition and returning to no flow [35]. For many basic research studies, the process of wind tunnel start/unstart can be used to represent the unstart process in a scramjet isolator [17] [52] [53]. Asymmetry in the normal shock structure has been seen in the experimental shadowgraph data as well as the CFD data for this study. Asymmetry in the starting shock of the wind tunnel has been well documented in the past in the literature as seen in Figure 3.3 [35]. There have been no documented reasons for this asymmetrical nature despite the symmetrical nature of wind tunnel nozzles, as seen in *Shock Wave Boundary Layer Interactions* by Babinsky [35].

Shock Train Dynamics

The shock train is the primary flow feature in an isolator. Figure 3.4 shows a shock train structure for normal shock trains. This structure begins with a normal SBLI as the initial shock in the shock train. After the first normal shock with its dual lambda structure, there is a section of reaccelerating flow seen in grey on the diagram. Then there are several more normal shocks without the lambda structure. They are weaker than the initial shock and have decreasing amounts of reaccelerated flow. These get smaller the further down the shock train as boundary layer separation increases. Eventually, the flow cannot recover to supersonic speeds and the flow moves into the mixing region where there is a channel of supersonic flow in the subsonic region [17] [15] [52]. The shock train and the mixing region are typically similar in length [53] .

Other shock trains that occur are oblique shock trains, which have oblique shock interactions rather than normal interactions throughout the isolator. The type of shock train is determined from two main factors: the confinement ratio of the wind tunnel and the Mach number. Figure 3.5 shows several historical shock train studies plotted by Mach number and confinement ratio, the formula chosen for square or axisymmetric tunnels. These experiments are added to the chart with a purple x. This puts these experiments solidly in the transitional range. This led to more uncertainty in the experimental design of the model since different types of shock trains have different length scales [24].

The shock train has been studied in the literature [54] [53] [17] to determine many of its fundamental features. The work by Hunt et al. characterized the transient nature of the shock train as a function of back pressure [17]. This work also characterized the 3D nature of the shock train with Particle Image Velocimetry. The work of Vandstone et al. sought to employ a closed loop control system to mitigate an unstart event based on the response to a change in pressure [53]. CFD studies have focused on the impact of inflow boundary layer variations [49] and turbulence model [55] in the uncertainty of an unstart event. However, there is still a large gap in the literature for joint computational and experimental studies. As mentioned previously, there are countless benefits to these joint studies [13] in helping further understand the fundamental nature of an unstart event.

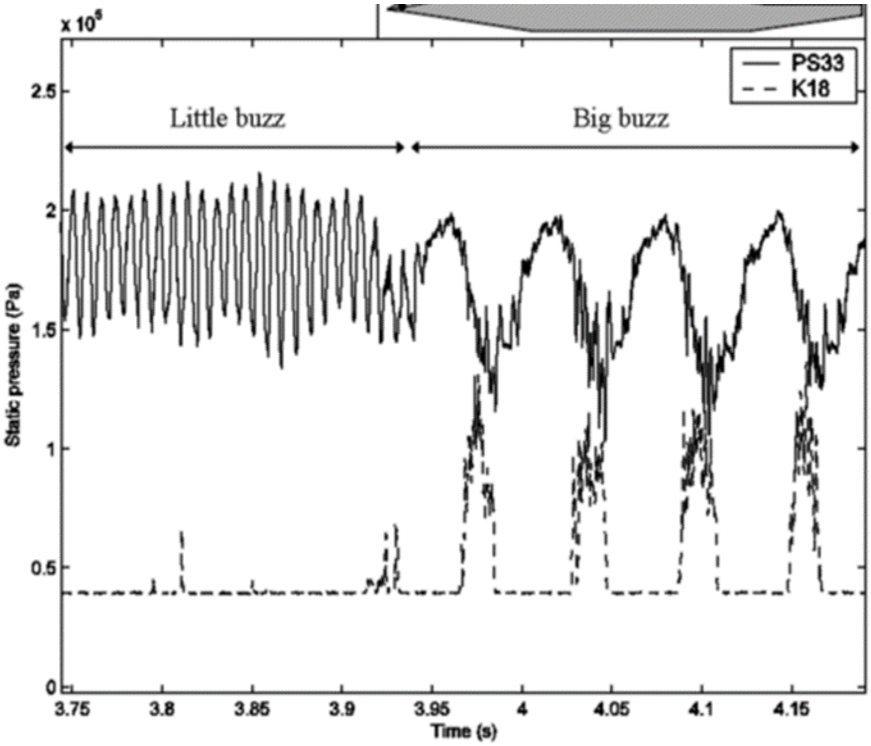

Figure 3.2. Oscillation of unstart shock in little and big buzz mode. [51]

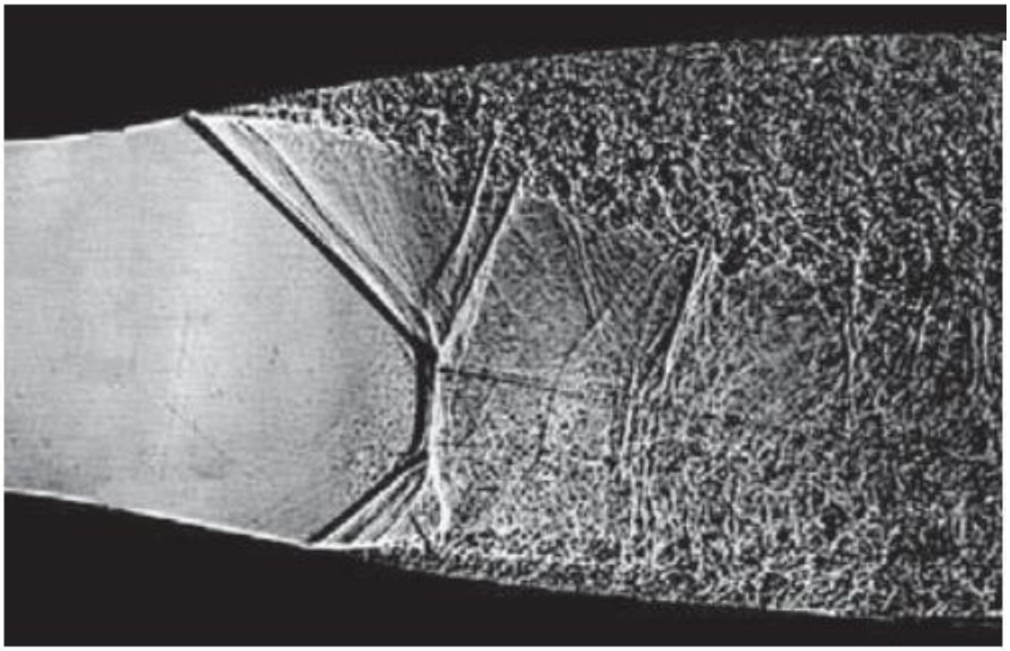

Figure 3.3. Nozzle starting at Mach 1.6 with asymmetric normal SBLI. [35]

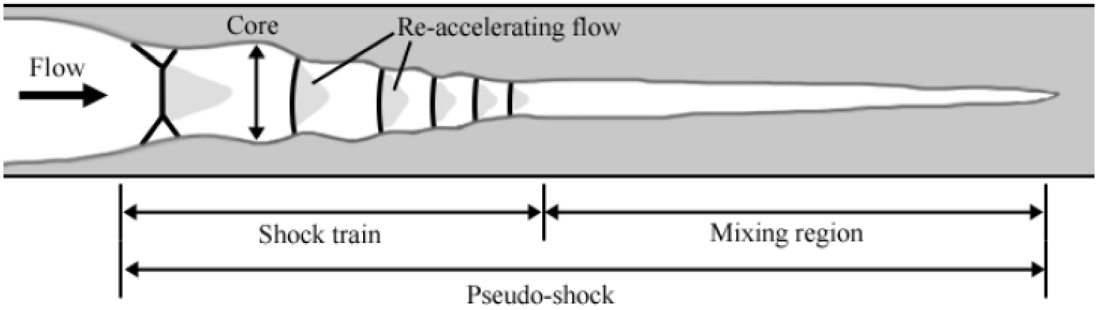

Figure 3.4. Shock train structure [17]

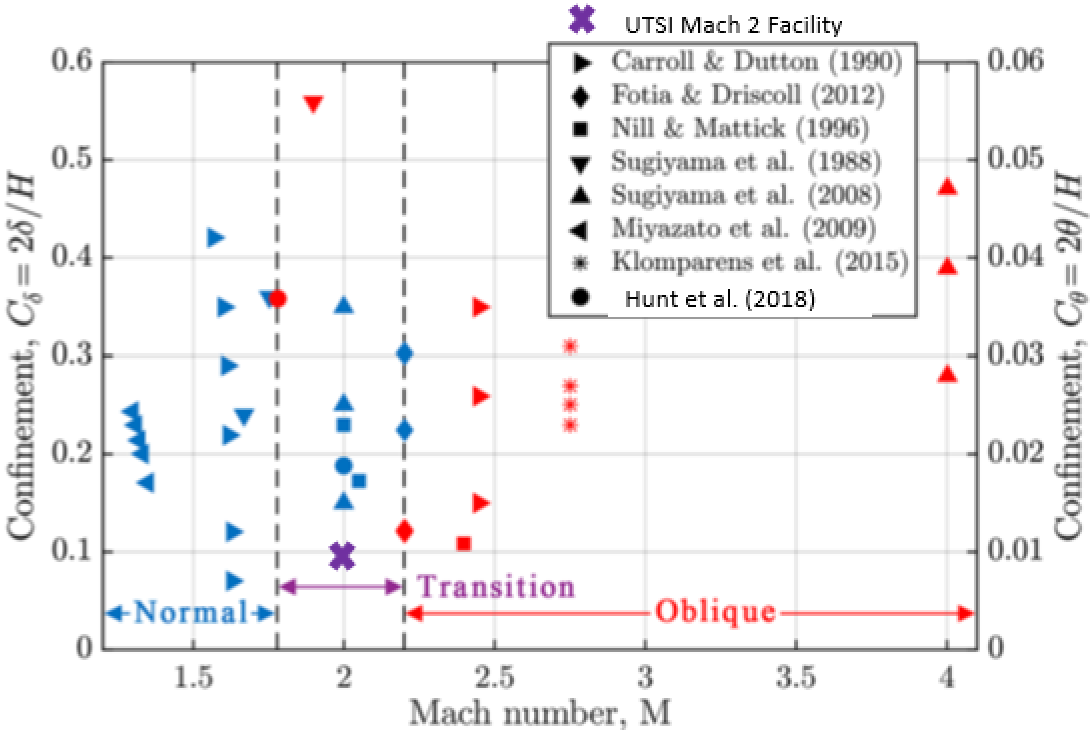

Figure 3.5. Plot showing the type of shock train based on tunnel geometry and Mach number [17]. The UTSI Mach 2 facility has been added as the purple x.

Experimental Set Up and Diagnostics

Model and Actuator Design

A dynamic cylinder model was designed to provide a variable-height cylinder to change the area blockage during a wind tunnel run. The 2.54 cm (1 in) diameter cylinder was run through the test section ceiling and actuated via a linear actuator mounted above the wind tunnel. This system allowed for area blockage changes during the wind tunnel run which moved the tunnel between unstart and started states. This type of model offered several advantages over those typically seen in the literature, butterfly valves and moving ramps [17] [54]. For a test section the size of the Mach 2, a ramp would be far too large to actuate with economical motors. The butterfly valve would require major installation into the tunnel and a large expense for the large size of blockage needed. Thus, the cylinder design was economical as it used a simple 1 in. cylinder and preexisting hardware. The ceiling of the wind tunnel already had access ports where the cylinder could enter the tunnel easily. A rendering of the cylinder and its mounting hardware can be seen in

Figure 3.6.

Figure 3.7 shows the linear actuator and mounting set up used to move the cylinder during the wind tunnel run. The cylinder can be seen mounted via a L bracket to the actuator. The actuator was a Velmex Stepping Motor Controller with a PK266-03B motor. This was mounted to the single-axis BiSlide assembly from Velmex. The cylinder was attached to the mounting plate on the actuator and moved using COSMOS software. The motor was run at maximum speed which changed as a function of pressure on the cylinder face.

The dynamic cylinder system was installed in the third test section as predicting the length of a shock train is approximated at 10-20 duct heights [24]. This allowed the maximum amount of room to move the shock train in the test section. However, the final results showed that the shock train stayed confined to two test section lengths.

Full Diagnostic Set Up Suite

Figure 3.8 shows a mockup of the entire diagnostic suite used for these experiments. This represents the ideal design of the experiment, not the final results. The black bars on the outside of the image represent the wind tunnel walls, and the image inside is the desired flow field of the shock train. The cylinder location is shown at the end of the wind tunnel test section representing the third test section block. The first yellow rectangle represents the Schlieren imagining section in the first test section. This was acquired at 50 Hz. The second yellow rectangle represents the retroreflective shadowgraph imaging section in the third test section. Retroreflective shadowgraph was chosen as it allows for a very simple optical set up that would not interfere with the z type Schlieren set up. This was imaged at 50 Hz as well with the two cameras for the optical measurements synchronized to each other. This allowed the maximum amount of the wind tunnel to be visualized during the run. Since creating an unstart state in the wind tunnel is inherently off condition, being able to react swiftly to any complication was critical.

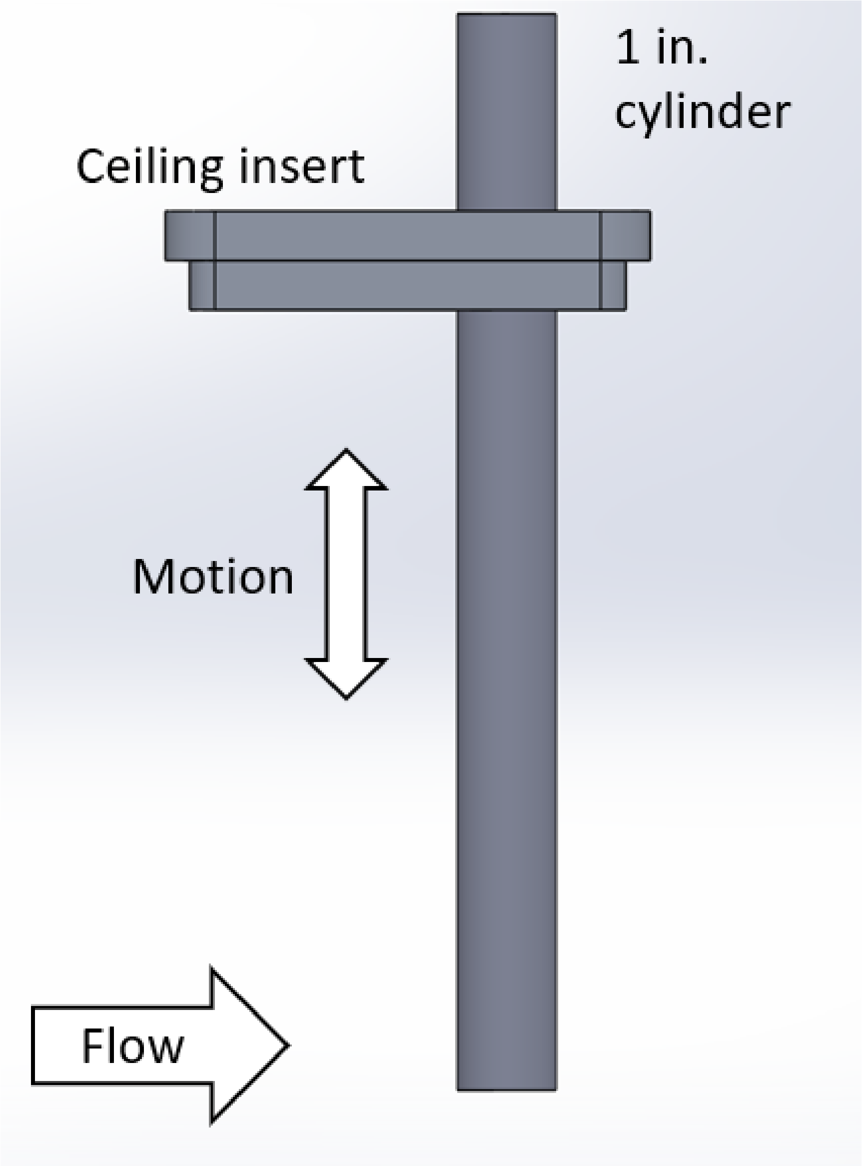

Figure 3.6. Rendering of cylinder and ceiling insert.

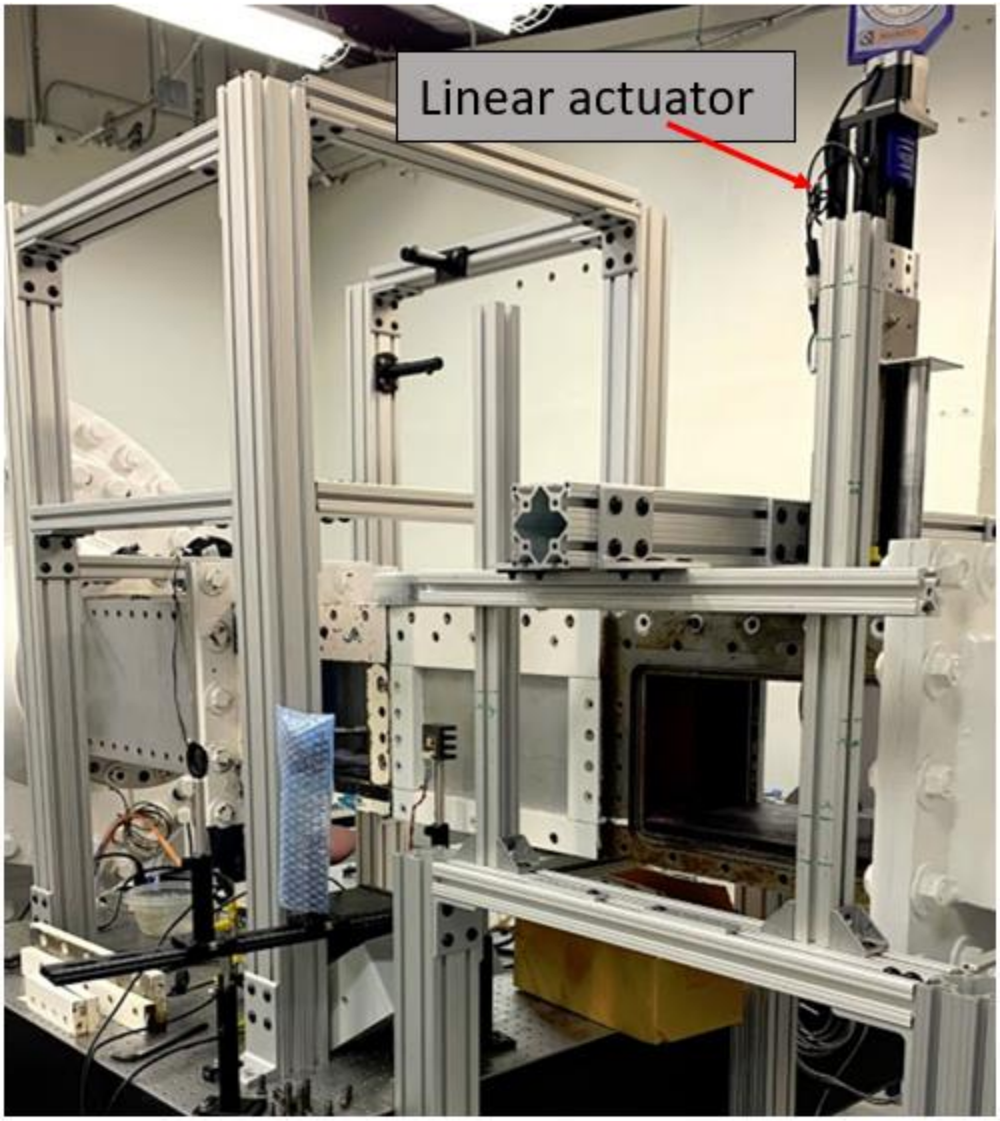

Figure 3.7. Linear actuator mounted in the third test section.

The tunnel is also equipped with pressure transducers along the tunnel centerline from which data was recorded. However, due to various circumstances only a handful of the transducers provided accurate data. This severely limited their usefulness for this experiment. In additional test runs after the shock train location was found to be in the third test section, the image acquisition rate was increased to 10 kHz for the retroreflective shadowgraph imaging. Additional technical details about this set up are in the following section as it was the primary diagnostic.

Retroreflective Shadowgraphy

A schematic of the retroreflective shadowgraphy setup is shown in Figure 3.9. The light source was a high-powered, pulsing, white light-emitting diode (LED) system developed in-house at UTSI. The LED's pulse characteristics were controlled by a DG 535 delay generator with a typical pulse width of 0.7 µs for a frequency of 50Hz and 10 kHz. An achromatic lens focuses the light onto a rod mirror with an angled face at 45° to redirect the light perpendicular to the incident optical axis. RTV silicone secured rod mirror to a transparent 55 mm filter to allow the mirror to be concentric with the camera lens. In the original method developed by Edgerton [56], the light source was slightly off-axis with respect to the camera, resulting in a distorted image. Figure 3.9 illustrates the rod mirror technique to keep the light source in-axis with the camera without an intensity reduction. A 2 ft × 2 ft segment of retroreflective material (3M^{TM} Scotchlite^{TM} High Gain Reflective Sheeting) was placed on the far side of the tunnel and perpendicular to the centerline of the camera. The retroreflective material provides increased sensitivity when compared to shadowgraph systems using plain white backgrounds, as 3M^{TM} reports a luminance factor 900 times greater with the retroreflective material.

A Photron FASTCAM Mini UX-100 and AX-200 high-speed cameras were synchronized with the LED. The camera's electronic shutter was set to 1 µs, using approximately 90% of the LED illumination for image exposure. High-speed images were captured at 10 kHz with a resolution of 512 × 384 pixels. This provided sufficient spatial and temporal resolution to capture and identify the critical flow features. The LED was operating during the entire wind tunnel operation, but a manual trigger was used to record the data after the shock train had been created.

Results

This section outlines the results for the unstart investigation. The primary diagnostic shown is the results of the shadowgraphy. While Schlieren and pressure data were acquired, the shock train did not enter the field of view of the Schlieren and several pressure taps were nonfunctioning, which limited the usefulness of the pressure data. Thus, the results from these diagnostic techniques are not presented in this document. The presented results include shadowgraph data proving the success of the experiment in creating a shock train, which was one of the main objectives for this experiment. The images were then analyzed to acquire quantitative data investigating the asymmetrical nature of the shock train, which addressed the other main question of the experiment.

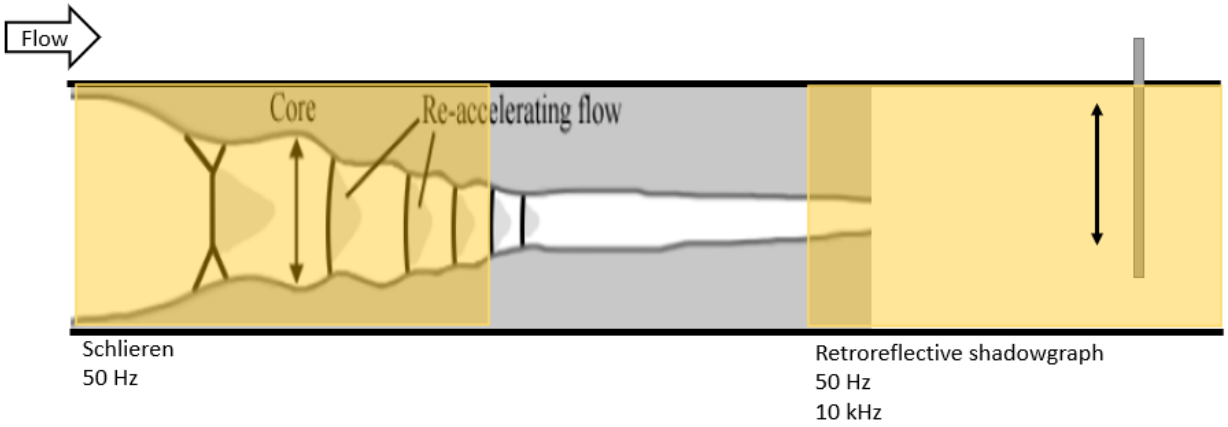

Figure 3.8. Schematic shows the flow features that is created with the actuated model and imaging diagnostics.

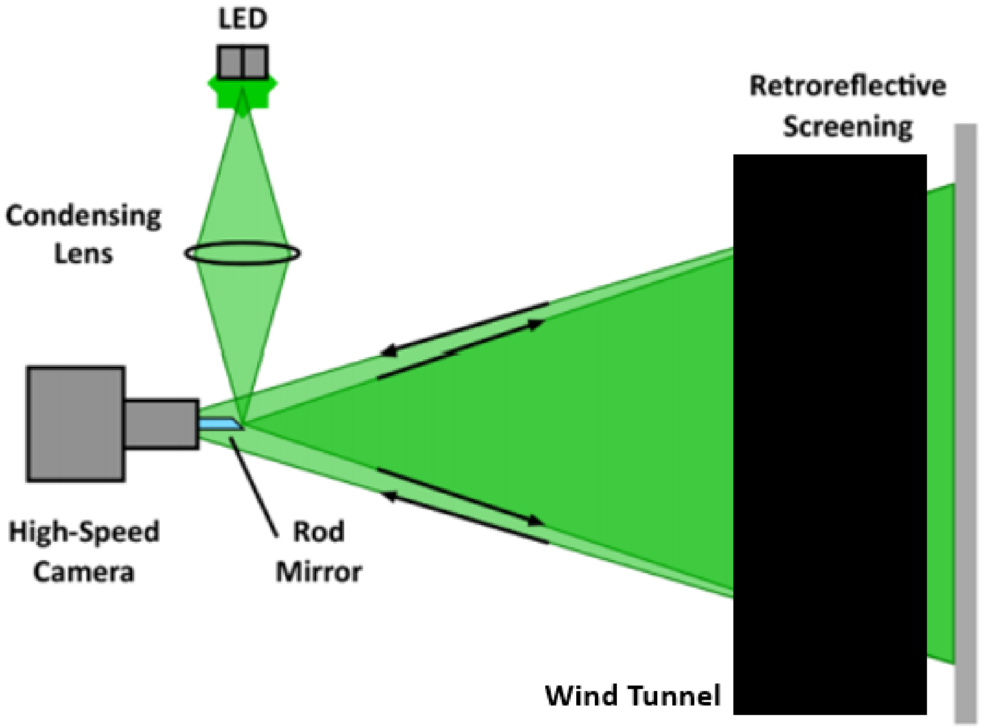

Figure 3.9. Retroreflective shadowgraphy schematic. Adapted from Schwartz et al.

Shock Train Generation

One of the major questions in the diagnostic selection for this experiment was if the retroreflective shadowgraph would be sensitive enough to capture the shock train. The shadowgraphs did capture the entire shock train and the boundary layer. This proved sensitive enough to determine all required flow features to decide if the model design was successful. Figure 3.10 below shows the tunnel during the entire run moving from a fully started flow to a state of unstart with the shock train pushed upstream of the dynamic cylinder. Note the white cluster of circles near the center of the image are light glares of the LED light through both sides of both pieces of glass.

The image sequence clearly shows the wind tunnel being fully started as the starting shock of the wind tunnel moves through in image a) and then the Mach waves can be seen in image b) showing started flow. Images c) and d) show the cylinder protruding down into the tunnel which causes an SBLI to appear and grow larger eventually impinging upon the floor in image d). Then, the tunnel moves to a state of unstart in image e). In image e), the unstart shock appears, which mimics the structure of the starting shock of the wind tunnel. Next, in image f), the shock train is visible, and its leading shock moves upstream out of the field of view. This was the goal of the model design: to create a shock train and be able to move it by changing the height of the cylinder, i.e. the backpressure.

After the ability of the model to create a shock train and the retroreflective shadowgraph's ability to capture the flow features were proven, additional data was taken at 10 kHz. This provided time resolved data [17] for the shock train while still having a large enough field of view to image all pertinent flow features. In Figure 3.11 the montage shows images sequenced from the 10 kHz acquisition with contrast and brightness enhanced for shock train visibility. This shows the movement of the shock train at high speeds as the images shown are 100 µs apart. Thus, the retroreflective shadowgraph diagnostic technique can capture the shock motion at time resolved speeds as well.

Asymmetrical Nature of the Unstart Shock

The starting shock of a wind tunnel has been noted to be asymmetrical in nature [35] as previously mentioned. This can be seen in the starting shock of the wind tunnel captured during this study, seen in Figure 3.12. This asymmetry was also noticed in the corresponding unstart simulations for this study. These simulations modeled the unstart shock propagating upstream after the change in conditions to induce unstart and it was noted to be asymmetric. After this asymmetry was noticed in the simulations, the experiments were also consulted to see if there was a physical nature to the asymmetry. Figure 3.12 and Figure 3.13 shows that the asymmetry can be seen both the starting and unstart shock in the experimental data. Thus, additional analysis was undertaken to further investigate the nature of the asymmetry. Note that the top boundary layer and approximately 2 inches of the test section are not visible in Figure 3.12 or Figure 3.13 and the orange line marks the centerline of the test section to highlight the asymmetry. In these figures, it can clearly be seen that the midpoint of the Mach stem is below the centerline of the wind tunnel.

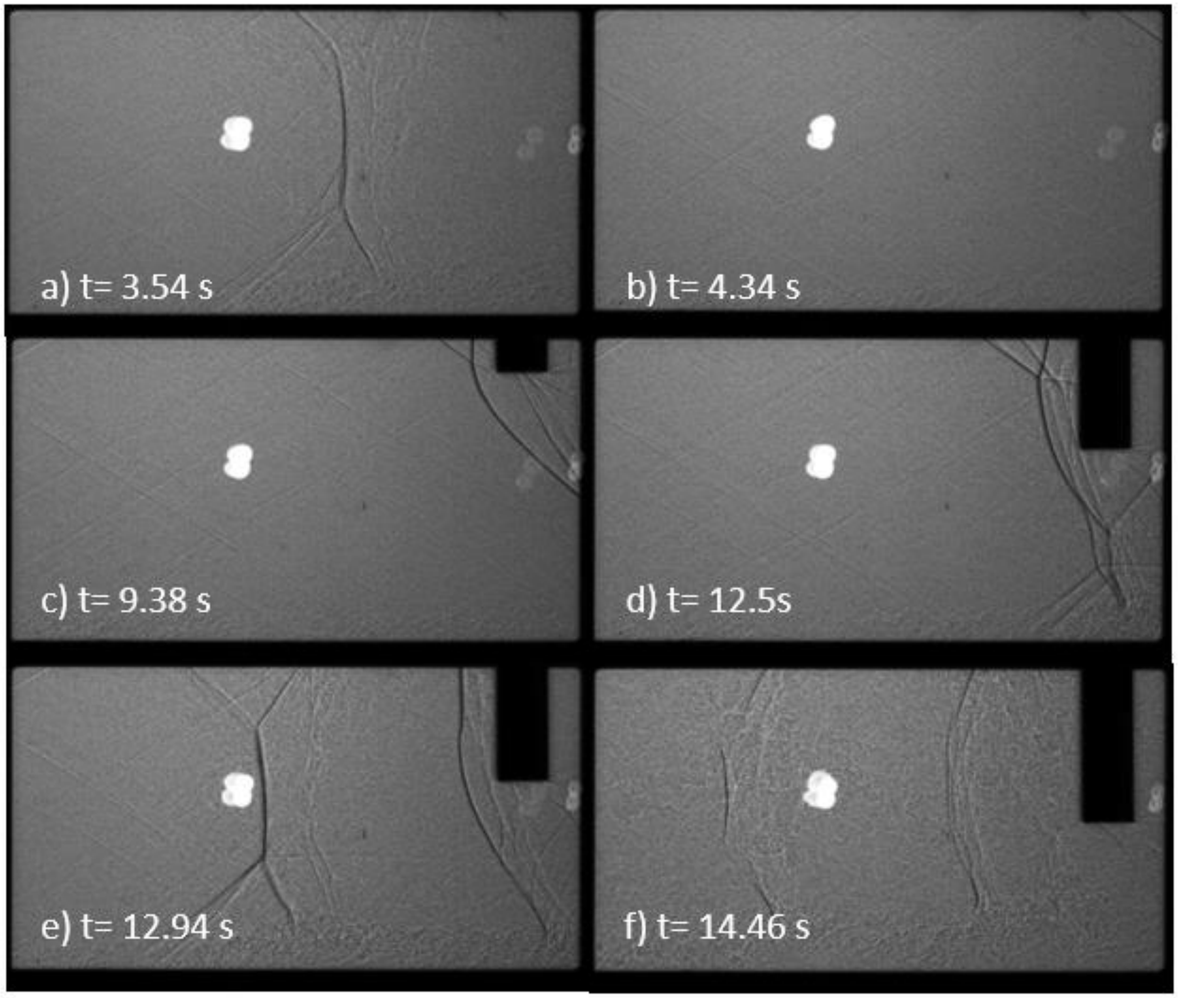

Figure 3.10. Image sequence showing the tunnel moving from a started to unstarted state at 50 Hz. Flow is left to right.

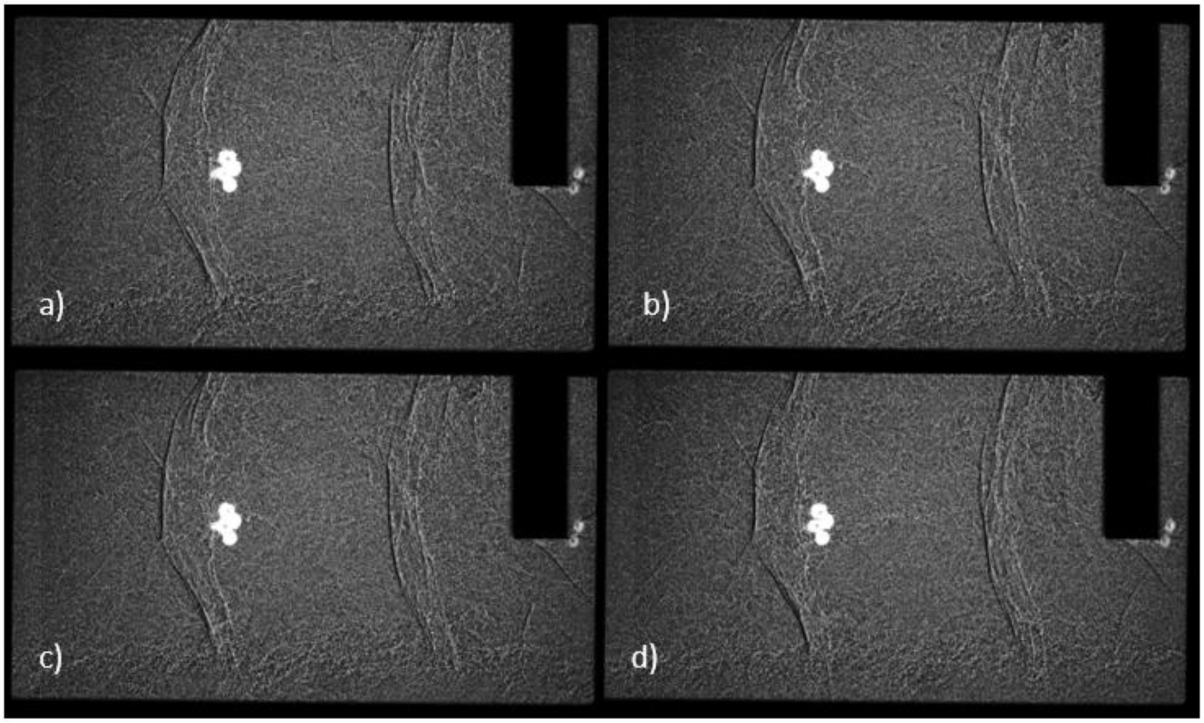

Figure 3.11. Image sequence showing the movement of the shock train at 10 kHz. Flow is left to right.

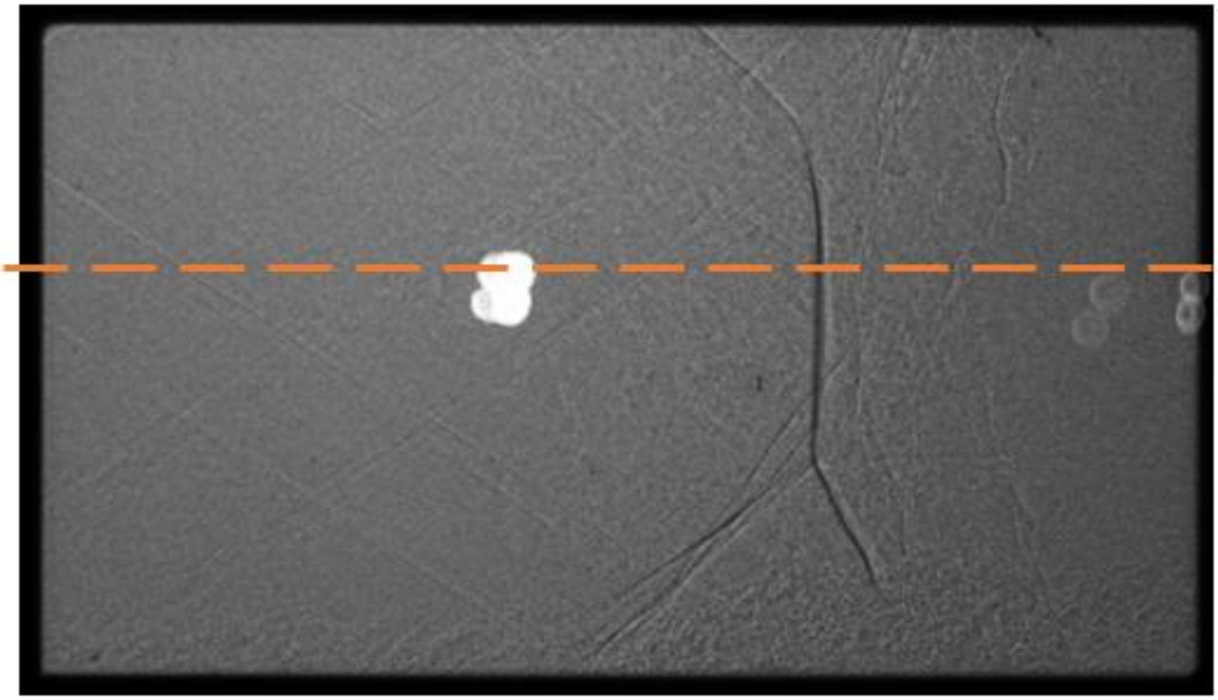

Figure 3.12. The starting shock of the wind tunnel with the centerline of the tunnel marked with an orange line.

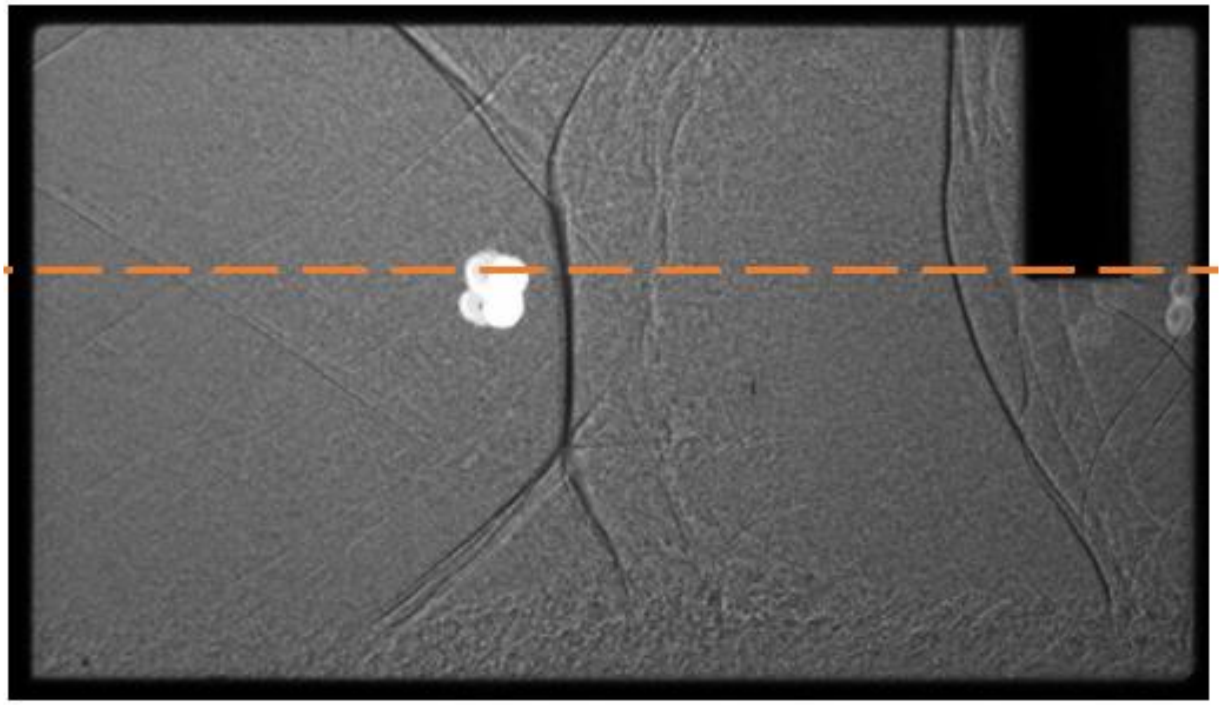

Figure 3.13. The initial unstart shock as the tunnel moves to an unstart condition with the centerline of the tunnel marked with an orange line.

The starting shock of the wind tunnel was analyzed for asymmetry in the same test run as the unstart shock. The pertinent flow features are shown in Figure 3.14 on a representative image of the unstart shock. The wind tunnel centerline is represented by the orange dashed line. The ceiling triple point and the floor triple point (both shown in white) are where the lambda structure of the normal SBLI begin with respect to the pertinent boundary layer. The Mach stem midpoint, shown in red, is the middle of the Mach stem calculated by taking the difference between the two triple point locations. The distance from the centerline is shown in blue and is measured by subtracting the Mach stem midpoint from the wind tunnel centerline location. The location of the shock is determined by measuring the distance from the Mach stem to the front face of the cylinder. This is fairly intuitive for the unstart cases, but the start cases have some locations past the cylinder face as it is not present for the starting shock to propagate downstream.

Figure 3.15 shows the Mach stem size of the starting shock of the wind tunnel by time. The error in these measurements is ±4 pixels, which is ±0.05 inches. All distances were normalized by the half height of the wind tunnel, 4 in. Some of the lower outlier points represent images where the upper triple point height was not visible as there was no lambda structure, but the Mach stem did curve significantly. This point of curvature was taken as the triple point height. Note the shock motion captured in the starting shock data set represents 1.44 seconds.

The same data is also shown in relation to the location of the Mach stem in the wind tunnel in Figure 3.16. Since the shock moves back and forth, this shows the trend of the Mach stem length for each specific location rather than when it occurred. The 0 point is the front face of the cylinder. For the start data, some points are behind the front face of the cylinder as it was still retracted. There is a greater range in Mach stem size as the starting shock moves closer to the end of the tunnel.

For additional characterization of the asymmetry, the Mach stem midpoint was found and the distance of the midpoint from the centerline of the tunnel was calculated. Figure 3.17 shows the distance from the centerline as a function of location in the wind tunnel. The midpoints all fall below the centerline of the tunnel suggesting a thicker separation region on the ceiling of the tunnel. Thus, the asymmetrical nature is completely skewed below the centerline. The ceiling area is not completely visible due to the optical access limitations of the facility. However, this is consistent with what is seen in the literature as seen in Figure 3.3, where the ceiling lambda structure and boundary layer was much larger than the floor structure [35].

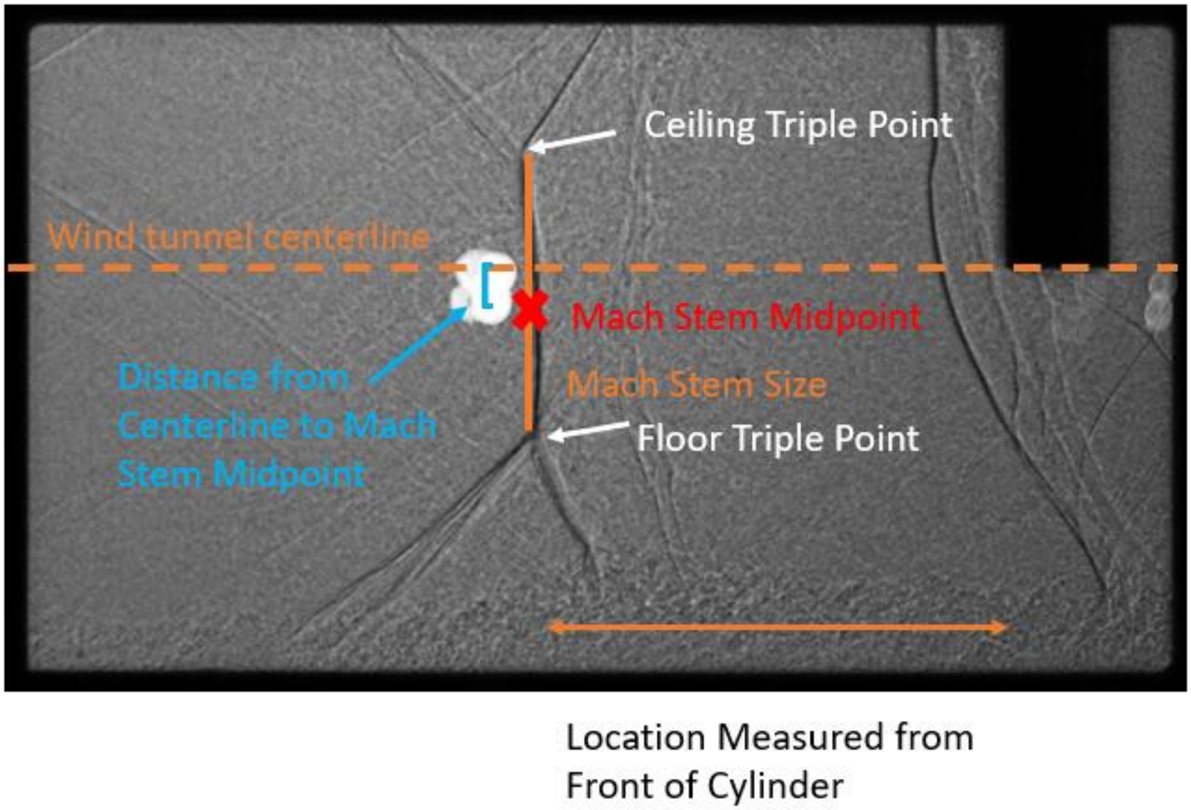

Figure 3.14. Measured flow features of the shock train for the asymmetry study.

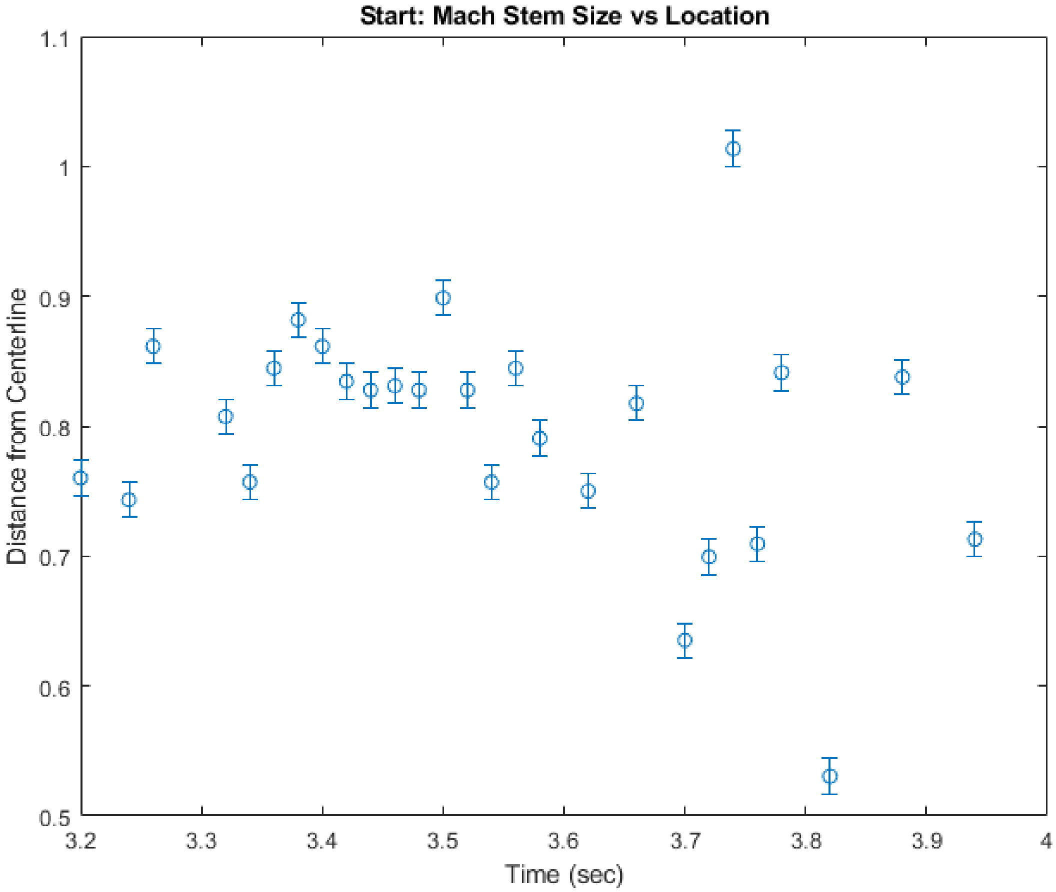

Figure 3.15. Mach stem length versus time for the starting shock of the wind tunnel.

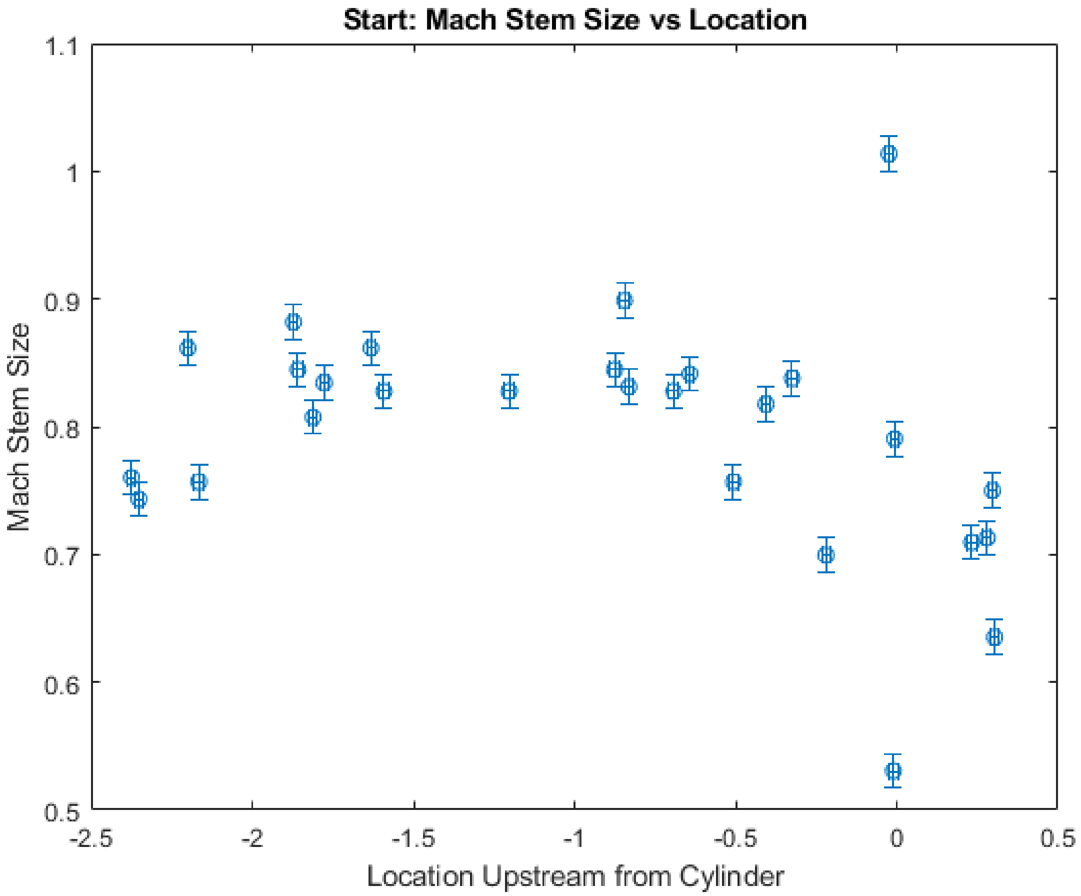

Figure 3.16. Mach stem height vs location in the wind tunnel shown as distance from the cylinder face.

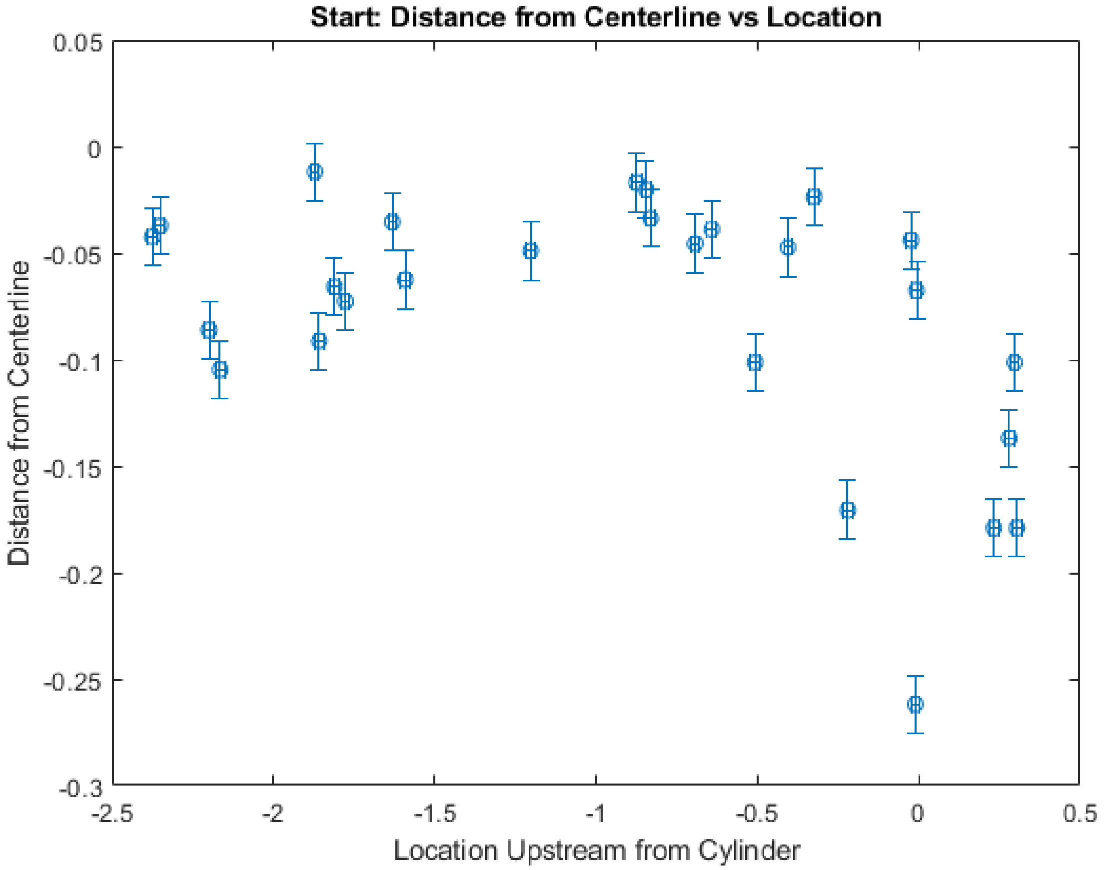

Figure 3.17. The distance from the Mach stem midpoint from the centerline of the tunnel normalized by the tunnel half height.

To additionally characterize the spread of the distance from the centerline data, the data is shown as a histogram in Figure 3.18. This shows that the bulk of the data is minimally asymmetric as most values fall between [-0.05, -0.01]. However, there are still some highly asymmetrical cases, which are primarily those that occur further downstream. To better quantify the shape of the distribution, skewness and kurtosis are common metrics to mathematically quantify the distribution. The skewness of the data is -1.4, which is a measure of symmetry of the data. As can be seen in the figure, the data has a long left leaning tail which is quantified by the negative skewness value. The kurtosis of the data is 1.9, which quantifies the presence of outliers. A normal distribution has a kurtosis of 3, so the impact of the outliers is shown. As previously mentioned, there were several noted outliers, and this is reflected in the large kurtosis value. Time resolved data would help to further clarify this characteristic.

While the starting shock asymmetry has been documented in the literature, the unstart shock asymmetry was seen in the computational results for this set of boundary conditions. Thus, the question of if the asymmetry held into the unstart motion was still a major question to be determined from experimental data. This second set of data was taken of the initial unstart shock in the wind tunnel moving the flow from start to unstart as it moves upstream. The asymmetric nature was seen here as well. Additionally, the unstart shock has many of the same visual characteristics of the starting shock. This was data from the same wind tunnel run as the previous data and taken in the same way. The error is the same at ±4 pixels or ±0.05 inches. The shock motion captured in this data set represents 2.86 seconds.

The unstart analysis is shown in similar graphs as the starting shock data. Starting with Figure 3.19, the Mach stem size is shown as a function of location in the wind tunnel. The unstart shock data is much more concentrated in one location of the tunnel due to the slower nature of the cylinder changing the blockage area versus the initial transient process of the starting shock moving downstream. The outliers here can be easily seen to correlate with tunnel location, but overall, the data shows consistency.

For comparison to the starting shock data, the distance of the Mach stem midpoint from the centerline of the wind tunnel was plotted for the unstart data as well. In Figure 3.20, the distance from the centerline is plotted as a function of location in the tunnel. The same trend is seen for the unstart data as the start data since all the values are negative meaning the Mach stem midpoint is always below the tunnel centerline. Thus, the unstart shock is asymmetrical and has the same characteristics of a wind tunnel starting shock. This confirms the results seen in the computational data as well.

As the data in Figure 3.20 were mostly between 1 and 1.5 tunnel half heights from the cylinder, the data shows the variation of the SBLI at one primary location. This shows the real range of the asymmetry even without time resolved data. To determine if any other parameters may have an influence in this size range, the same distance from the centerline data is plotted versus time in Figure 3.21. There is no immediately obvious sinusoidal influence, but there is a more general bimodal nature to the data as the range is greater at the beginning and end in time of the shock motion captured.

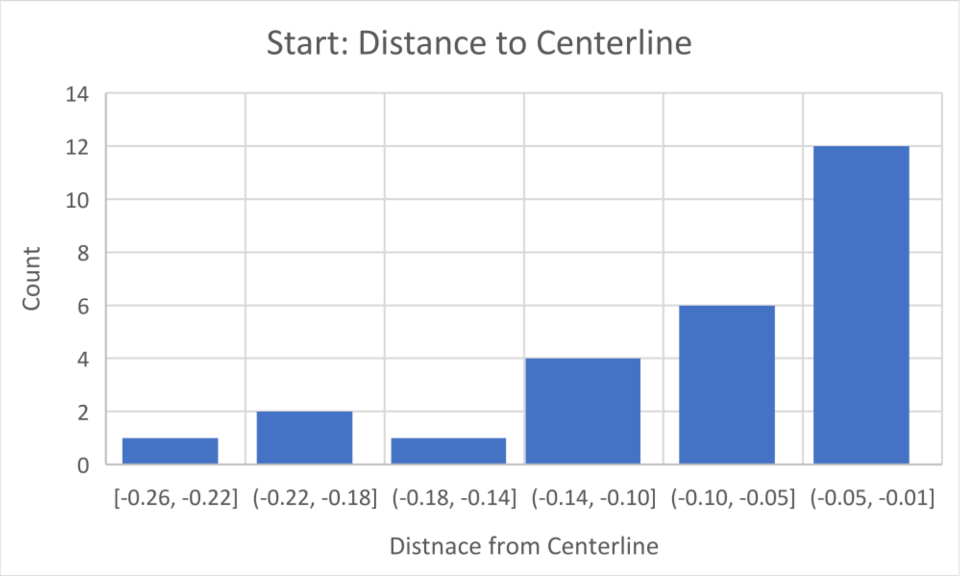

Figure 3.18. Histogram of Mach stem midpoint to the centerline of the wind tunnel for the start data.

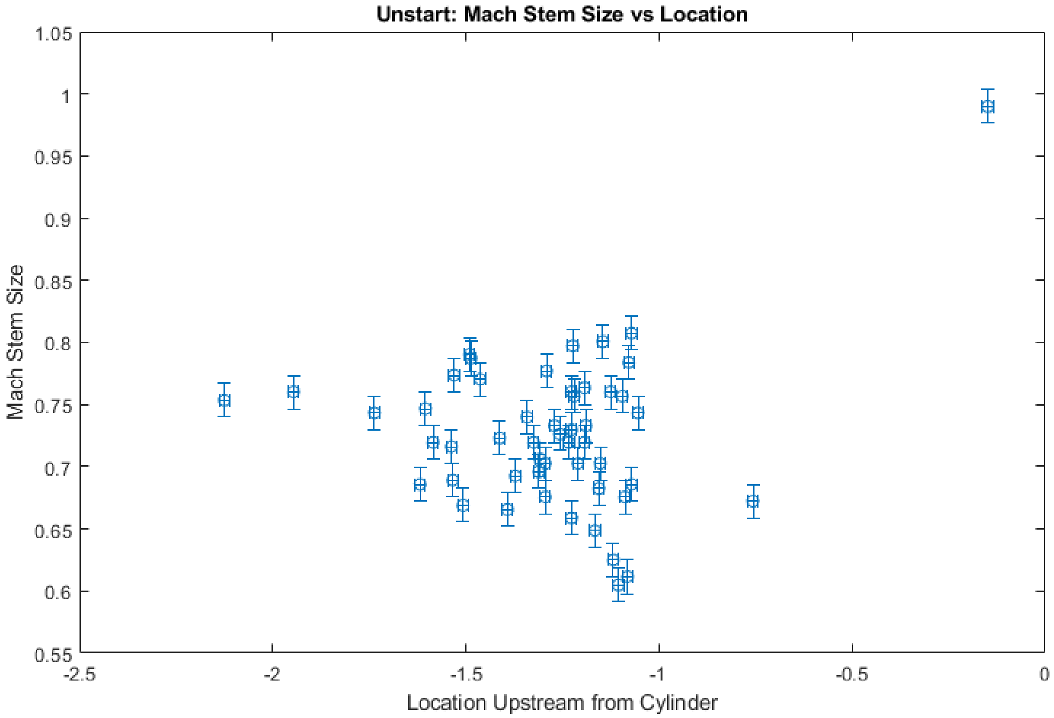

Figure 3.19. The Mach stem size versus location in the wind tunnel.

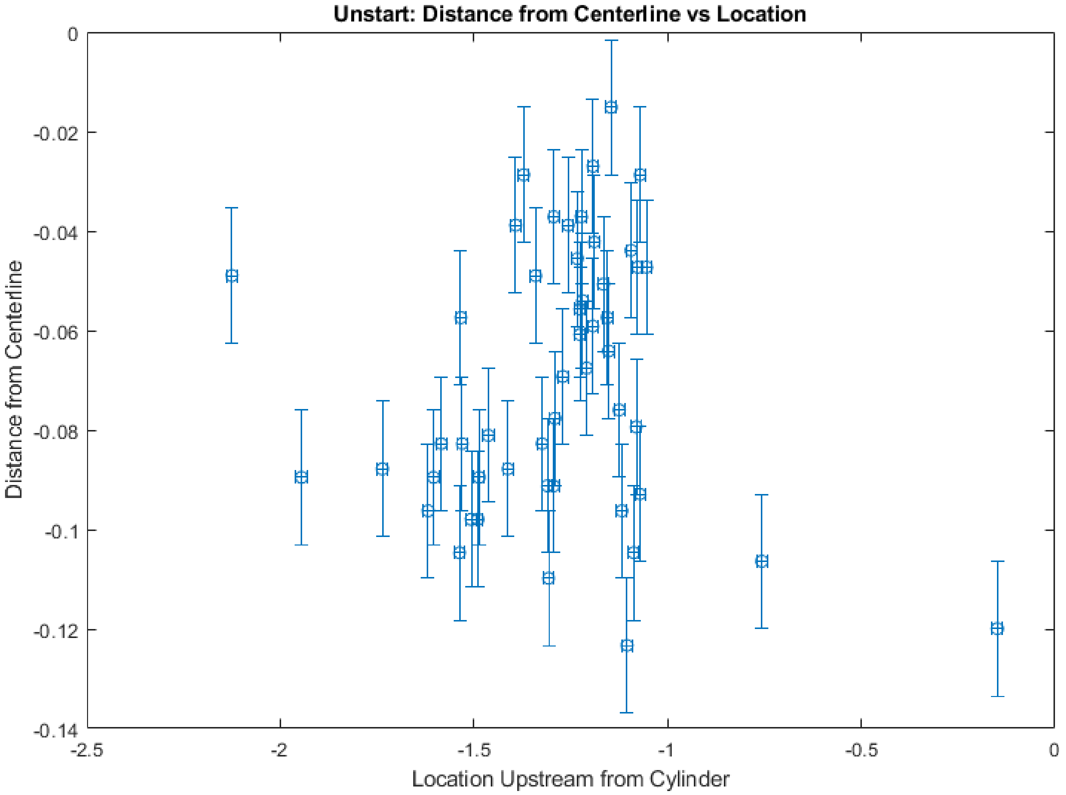

Figure 3.20. The distance of the Mach stem midpoint from the tunnel centerline normalized by the tunnel half height versus the location in the tunnel.

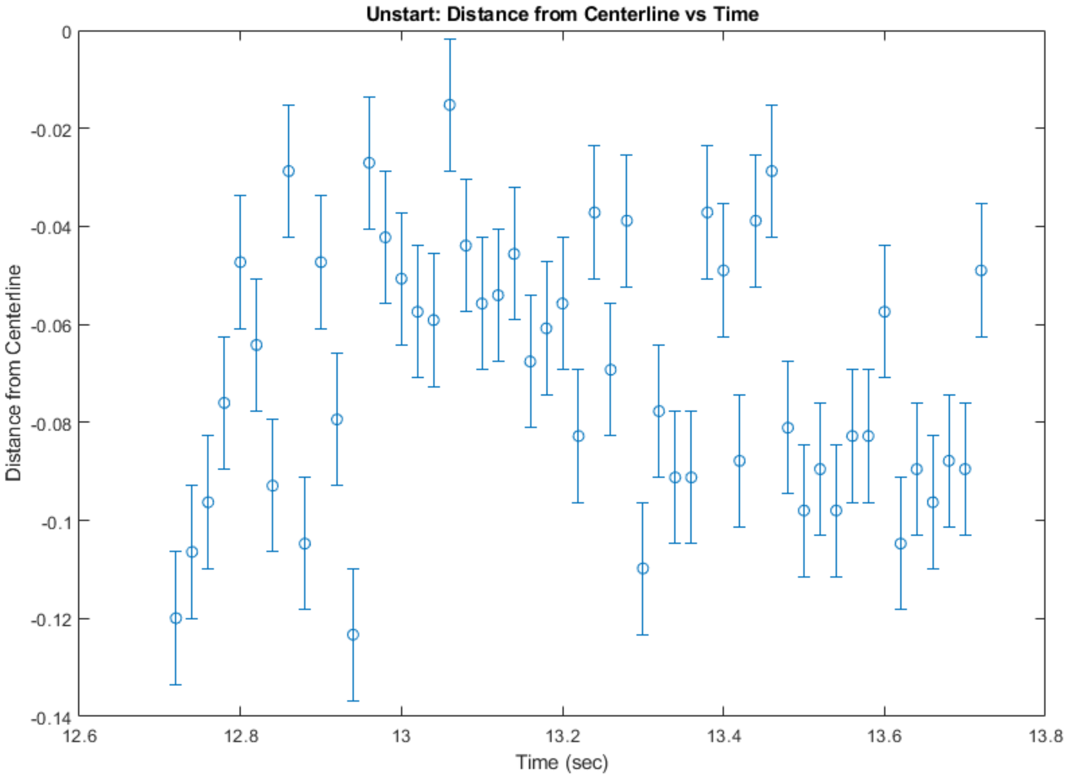

Figure 3.21. The distance of the Mach stem midpoint from the tunnel centerline normalized by the tunnel half height versus time.

To further investigate the bimodal nature seen in Figure 3.21 and compare to Figure 3.18 of the start data, a histogram of the distance from the centerline for the start data is shown in Figure 3.22. A distinct bimodal shape is seen, which does suggest more complexity in the unstart process. This does suggest there could be outside influences of the additional shocks in the shock train or the two competing forces of flow trying to move downstream from the tunnel throat competing with the flow moving upstream during the unstart process. The skewness and kurtosis were calculated for this data distribution as well. The skewness was 0 which shows that the two peaks are essentially equal and neither one is dominating the flow. The kurtosis was -0.9 and is considered platykurtic, meaning the distribution has very thin tails. The bulk of the distribution is condensed in a smaller range. There are still many unknowns in the asymmetry of starting shocks in general [35] and in the unstart process. This is an area of research that would greatly benefit from time resolved, bulk flow field studies.

Uncertainty Analysis

Potential sources of error in these measurements have already been addressed in relation to the data point acquisition of ±4 pixels, or ±0.05 inches. ImageJ [46] was used to make these measurements and ImageJ was designed for and has been used across many fields as a tool for image quantification and measurement [48]. The error in the measurement point is based on the size of the object compared to the pixel spread. Many of the flow features, as seen in Figure 3.14, were spread over several pixels and the error of ±4 pixels conservatively captures the spread. This error is reflected in the error bars on the figures relating to asymmetry and feature locations. There are error bars in the x and y axis of the graphs, but for most of the graphs, the x axis was a much larger physical distance so the error bars are mostly contained within the data marker.

The timing error is a function of the internal timing of the delay generator (DG535 by Stanford Research Systems) used to time the LED pulses and the camera shutter and is less than 1 ns [57]. This data is not time resolved, so there is a limit in what unsteady dynamics the data is capturing. A similar asymmetry analysis of time resolved data for the shock train would be useful in further understanding this behavior.

Other sources of error also exist in the irregularity of the wind tunnel size. It is assumed that the wind tunnel is a constant 8 in. by 8 in. but there is variability in its shape down the length of the test section. Additionally, the boundary layer height is referenced at 11 mm, but this measurement is from the first test section. The natural growth of the boundary layer would make it larger at the cylinder location. For future experiments, a new boundary layer measurement at the point of interest would be necessary.

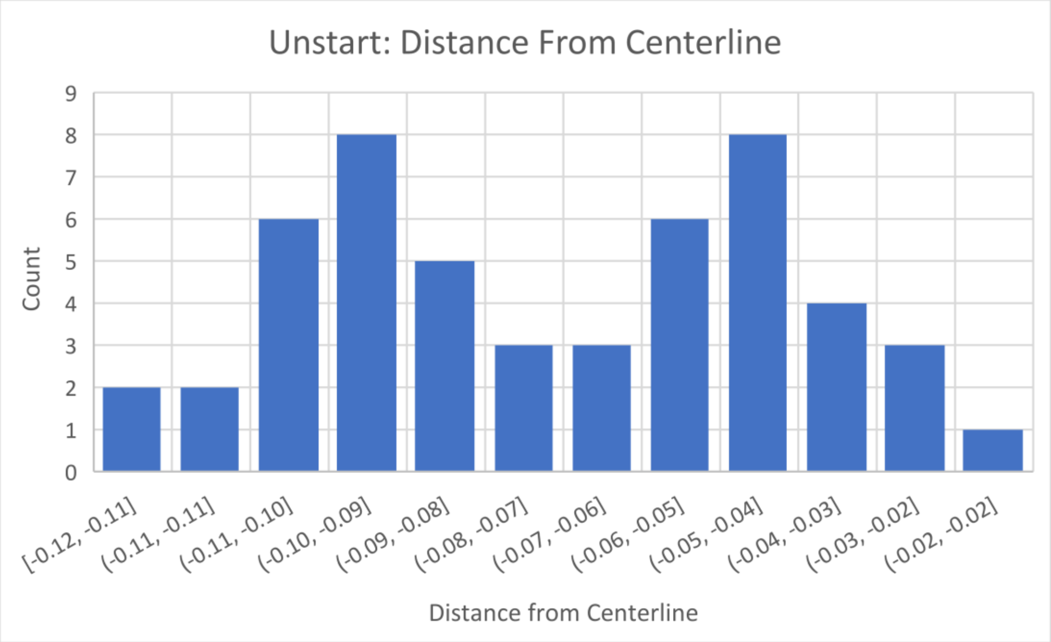

Figure 3.22. Histogram of Mach Stem midpoint distance to the centerline for the unstart data set.

CHAPTER FOUR

CONCLUSION

The universe is made of stories, not of atoms. – Muriel Rukeyser

The work presented within this document represents two separate experimental campaigns which worked to determine operating limitations of a scramjet flow path. The objectives of the two studies, as outlined in the Research Questions section of Chapter 1, were met as seen in the Results section of this document. This chapter discusses the overall conclusions drawn from each separate experiment and potential areas for future study. These results investigate the mitigation of off condition effects in a scramjet flow path by studying the ability to push separation downstream in an inlet type flow path and the ability to create a shock train and manipulate it via a dynamic cylinder.

Crossing Shock-Wave/Boundary-Layer Interaction Experiment

The Crossing Shock-Wave/Boundary Layer Interaction experiment showed that the addition of vortex generators as passive flow control can push back the separation point of the flow. The optimized case was found to be the x_S=3.75 in. VG case with 3 VGs placed on the test section floor. The x_S=4.75 in. case had less of an effect on moving back the separation point and the x_S=2.75 in. case had a negative effect on the separation location. This VG's ability to push separation further downstream could be useful to mitigate an unstart event if the separation location is one of the primary off flow conditions. However, the introduction of blockage via the VG's protuberances to the flow path has additional effects: the total pressure recovery is decreased as seen in the CFD results. This bulk flow effect does have an impact in the operation efficiency of the vehicle and would be up to the specific case which effect would be worse. Limited efficiency is not ideal but preventing an unstart case could prevent the total loss of the vehicle. This study shows that there can be benefit to such passive flow systems, but further study is required to fully characterize the total effect of the VGs on the bulk flow.

The study also showed good agreement between the experimental and computational cases. The percent difference in the computational and experimental separation locations was within the experimental error. This showed the ability of the Kestrel to match the baseline case, an internal flow, and match the effect of the VGs. This was a major question of the study and was found that there was a strong match in both the quantitative separation location and the qualitative streamlines.

Additionally, the Mach 2 interaction was not a strong enough interaction to see the more complex flow features present in the interaction at higher Mach numbers [30]. Thus, there are still questions of whether or not the code can reproduce the stronger interaction results, especially with the addition of the VGs. Additional cases at a higher Mach number would be necessary in determining the effect of the vortex generators more fully. The computational work done by Matthew Schwartz investigates some higher Mach number cases building on the work done in this study and presented here [22].

The effect of the sidewall boundary layer is shown through the analysis of flow angles in comparison to the work courtesy of Douthitt et al. and Arora [33]. The sidewall boundary layer moves the separation location downstream in comparison to measurements taken of a fin generated interaction in clean flow. This mimics the effects created by the vortex generators. Thus, the addition of the sidewall boundary layer can be used to move separation downstream as well, but the experiments in this study did not measure the other potential negative effects. Thus, further study is required to show the full effects of the sidewall boundary layer on a fin generated SBLI.

Unstart Experiment

The Unstart investigation produced a shock train in a representative isolator flow path. This proved that a shock train can be generated in the UTSI Mach 2 facility using a dynamic cylinder model. The dynamic cylinder model can mimic the changing backpressure conditions that could potentially create an unstart event in a typical scramjet flow path. The design of this type of model took inspiration from the literature of butterfly valves [17] and ramps [54] and adapted it to a larger test section size. Additionally, the retroreflective shadowgraph can also be used to capture time resolved data of the shock train. The work with the other diagnostics also helped prepare for pressure transducer placement and optical diagnostic placement. This experiment design and model construction lays the groundwork for additional studies to characterize the effect changing backpressure and boundary layer shape factor have on the dynamics of a shock train. The experimental data can then be used to inform uncertainty quantification around unstart [19]. This additional investigation is currently being done at UTSI and future publications from the HORIZON Research Group will showcase the results. These studies can help determine the uncertainty around unstart and apply it to future mitigation of unstart events.

The experiment also showed the inherent asymmetrical nature of the initial unstart shock in a shock train. This corroborated the results seen in the corresponding computational study [19]. The initial results from the computational study are shown in Acharya et al. [19] and further work, including the asymmetry investigation will be published in the future. Having the ability to check results with computational and experimental teams allows for additional insight into the fundamental physics. The Mach stem midpoint was shown to always be below the centerline of the wind tunnel for both the starting shock of the wind tunnel and the initial unstart shock generated by the cylinder. This is consistent with normal starting shock behavior seen in the literature [35]. The ability to confirm the asymmetry seen in the computations with experimental data shows the value of experimental/computational partnerships for these types of studies.

LIST OF REFERENCES

[1] T. M. Cronk, *Hypersonics, Counter-Hypersonics Are a Top Priority,* 2020.

[2] R. T. Vought and K. K. Droegmeier, "Fiscal Year (FY) 2022 Administration Research and Development Budget Priorities and Cross-cutting Actions," Executive Office of the President, Washington DC, 2020.

[3] J. D. Anderson Jr, Hypersonic and High-Temperature Gas Dynamics, Reston VA: American Institute of Aeronautics and Astronautics, 2019.

[4] J. D. Schmisseur, "Hypersonics into the 21st Century: A perspective on AFOSR-sponsored research in aerothermodynamics," *Progress in Aerospace Sciences,* 2015.

[5] J. J. Bertin and R. M. Cummings, "Fifty years of hypersonics: where we've been and where we're going," *Progress in Aerospace Sciences,* 2003.

[6] M. T. Klare, *An 'Arms Race in Speed': Hypersonic Weapons and the Changing Calculus of Battle,* 2019.

[7] H. M. Sayler, "Hypersonic Weapons: Background and Issues for Congress," Congressional Research Service, 2019.

[8] R. Speier, G. Nacouzi, C. A. Lee and R. M. Moore, "Hypersonic Missile Nonproliferation Hindering the Spread of a New Class of Weapons," RAND Corperation, Santa Monica CA, 2017.

[9] P. Ewing, "Arms race goes hypersonic," *Politico,* 11 08 2015.

[10] I. A. Leyva, "The relentless pursuit of hypersonic flight," *Physics Today,* November 2017.

[11] D. S. Dolling, "Fifty Years of Shock-Wave/Bounday-Layer Interaction Research: What Next?," *AIAA Journal,* vol. 39, no. 8, pp. 1517-1531, August 2001.

[12] G. S. Settles and L. J. Dodson, "Supersonic and hypersonic shock/boundary-layer interaction database," *AIAA Journal,* vol. 32, no. 7, pp. 1377-1383, 1994.

[13] J. A. Benek, "Experience with Validation Quality Experiments for Shock Boundary Layer Interaction," in *AIAA Paper 2014-0204*, 2014.

[14] J. J. Bertin, "Hypersonic aerothermodynamics," Washington DC, 1994.

[15] P. E. Rodi, S. Emami and C. A. Trexler, "Unsteady pressure behavior in a ramjet/scramjet inlet," *Journal of Propulsion and Power,* vol. 12, no. 3, pp. 486-493, 1996.

[16] D. V. Gaitonde, "Progress in Shock Wave/Boundary Layer Interactions," *Progress in Aerospace Sciences,* vol. 72, pp. 80-99, 2015.

[17] R. Hunt and M. Gamba, "Shock Train Unsteadiness Characteristics, Oblique-to-Normal Transition, and Three-Dimeensional Leading Shock Structure," *AIAA Journal,* vol. 56, no. 4, pp. 1569-1587, 2018.

[18] W. H. Heiser and D. T. Pratt, Hypersonic Airbreathing Propulsion, Washington DC: American Institute of Aeronautics and Astronautics, 1994.

[19] R. Acharya, P. Palies, J. Schetz and J. Schmisseur, "Development of Uncertainty Quanitification Framework Applied to Hypersonic Unstart Challenge," in *23rd AIAA*

International Space Planes and Hypersonic Systems and Technologies Conference , Montreal, Quebec, 2020.

[20] M. Schwartz, K. Stamper, R. Bond and J. Schmisseur, "Passive Flow Control on Crossing Shock-Wave/Boundary-Layer Interactions," in *AIAA Aviation 2019 Forum*, Dallas TX, 2019.

[21] "How Scramjets Work," NASA, 09 2 2006. [Online]. Available: https://www.nasa.gov/centers/langley/news/factsheets/X43A_2006_5.html.

[22] M. Schwartz, *A Numerical Study of the Scaling and Control of Distortion Caused by Crossing Shock-Wave/Turbulent Boundary-Layer Interactions,* 2019.

[23] J. D. Anderson, Modern Compressible Flow With Historical Perspective, McGraw Hill Education, 2003.

[24] J. S. Geerts and K. H. Yu, "Shock Train/Boundary-Layer Interaction in Rectangular Isolators," *AIAA Journal,* vol. 54, no. 11, 2016.

[25] B. D. Kocher, C. S. Combs, P. A. Kreth, J. D. Schmisseur and S. J. Peltier, "Investigation of the Effects of Distributed surface Roughness on Supersonic Flows," in *33rd AIAA Aerodynamic Measurement Technology and Ground Testing Conference*, Denver CO, 2017.

[26] B. E. Rice, N. J. Bisek, S. J. Peltier and J. W. Hofferth, "Investigation of Secondary Motion in High Speed Flow," in *55th AIAA Aerospace Sciences Meeting*, Grapevine TX, 2017.

[27] N. Titchener and H. Babinsky, "Shock Wave/Boundary-Layer Interaction Control Using a Combination of Vortex Generators and Bleed," *AIAA Journal,* vol. 51, no. 5, 2013.

[28] A. A. Zheltovodov and A. I. Maksimov, "Hypersonic Crossing-Shock-Waves/Turbulent Boundary Layer Interactions," Russian Academy of Sciences, Novosibirsk, Russia, 1999.

[29] M. I. Kussoy, K. C. Horstoman and C. Horstman, "Hypersonic crossing shock-wave/turbulent-boundary-layer interactions," *AIAA Journal,* vol. 31, no. 12, pp. 2197-2203, 1993.

[30] J. D. Schmisseur and D. V. Gaitonde, "Numerical Investigation of Strong Crossing Shock-Wave/Turbulent Boundary Layer Interactions," *AIAA Journal,* vol. 39, no. 9, 2001.

[31] E. Schulein and A. A. Zheltovofov, "Development of experimental methods for hypersonic flow studies in Ludweig tubes," in *International Conference on the Methods of Aerophysics Research*, Novosibirsk, Russia, 1998.

[32] M. C. Adler and D. V. Gaitonde, "Flow Similarity in Strong Swept-Shock/Turbulent-Boundary-Layer Interactions," *AIAA Journal,* vol. 57, no. 4, 2019.

[33] N. Arora, M. Y. Ali, Y. Zhang and F. S. Alvi, "Shock-Bounday Layer Interaction due to a Sharp Unswept Fin in a Mach 2 Flow," in *AIAA Scitech Forum*, Kissimmee Florida, 1-9 January 2015.

[34] F. S. Alvi and G. S. Settles, "Physical Model of the Swept Shock Wave/Boundary Layer Interaction Flowfield," *AIAA Journal,* vol. 30, no. 9, pp. 2252-2258, 1992.

[35] H. Babinsky and J. K. Harvey, Shock Wave Boundary Layer Interactions, Cambridge University Press, 2011.

[36] J. W. Barter and D. S. Dolling, "Reduction of fluctuating pressure loads in shock/boundary-layer interactions using vortex," *AIAA Journal,* vol. 33, no. 10, pp. 1842-1849, 1995.

[37] E. Baydar, F. K. Lu and J. W. Slater, "Vortex Generators in a Two-Dimensional External-Compression Supersonic Inlet," *Jounral of Propulsion and Power,* vol. 34, no. 2, pp. 521-538, 2018.

[38] T. Herges, E. Kroeker, G. Elliot and C. Dutton, "Microramp flow conrtol of normal shock/bounradry layer interactions," *AIAA Journal,* vol. 48, no. 11, pp. 2529-2542, 2010.

[39] F. Lu, Q. Li and C. Liu, "Microvortex generators in high-speed flows," *Progress in Aerospace Sciences,* vol. 53, pp. 30-45, 2012.

[40] D. C. McCormick, "Shock/boundary-layer interaction control with vortex generators and passive cavity," *AIAA Journal,* vol. 31, no. 1, pp. 91-96, 1993.

[41] J. W. Barter and D. S. Dolling, "Reduction of fluctuating pressure loads in shock/boundary-layer interactions using vortex," *AIAA Journal,* vol. 34, no. 1, pp. 195-197, 1996.

[42] M. Rybalko, H. Babinsky and E. Loth, "Vortex Generators for a Normal Shock/Boundary Layer Interaction with a," *Journal of Propulsion and Power,* vol. 32, no. 7, pp. 71-82, 2012.

[43] S. Lee and E. Loth, "Supersonic Boundary Layer Interactions with Various Micro - Vortex Generator Geometries," in *AIAA Paper 2009-3712*, 2009.

[44] S. Lee and E. Loth, "Impact of Ramped Vanes on Normal Shock Boundary-Layer Interaction,," *AIAA Journal,* vol. 50, no. 10, 2012.

[45] Emerson Process Managment, *ROSEMOUNT 1151 ALPHALINE PRESSURE TRANSMITTER SPEC SHEET,* 2009.

[46] C. A. Schneider, W. S. Rasband and K. W. Eliceiri, "NIH image to ImageJ: 25 years of image analysis," *Nature methods,* vol. 9, no. 7, pp. 671-675, 2012.

[47] R. H. Korkegi, "Comparison of Shock-Induced Two- and Three-Dimensional Incipient Turbulent Separation," *AIAA Journal,* vol. 13, pp. 234-535, 1975.

[48] J. M. Mateos-Perez and J. Pascau, Image Processing with ImageJ, Packt Publishing, Limited, 2013.

[49] R. Fivet, H. Koo, V. Raman and A. H. Auslender, "Numerical Investigation of Shock-Train Response to Inflow Boundary-Layer Variations," *AIAA Journal,* vol. 55, no. 9, 2017.

[50] Anon., *Schlieren Imaging of Supersonic Inlet Shocks,* NASA Glenn Research Center image gallery, 1955.

[51] S. Trapier, P. Duveau and S. Deck, "Experimental Study of Supersonic Inlet Buzz," *AIAA Journal,* vol. 44, no. 10, pp. 2354-2365, 2006.

[52] K. Matsuo, Y. Miyazato and H.-D. Kim, "Shock train and pseudo-shock phenomena in internal gas flows," *Progress in Aerospace Sciences,* pp. 33-100, 1999.

[53] L. Vandstone, A. Bosco, Y. Saleh, M. Akella, N. T. Clemmons and S. Gogineni, "Closed-Loop Control of Unstart in a Mach 1.8 Isolator," in *AIAA Scitech 2019 Forum*, San Diego California, 2019.

[54] J. L. Wagner, K. B. Yuciel, A. Valdivia, N. T. Clemens and D. S. Dolling, "Experimental Investigation of Unstart in an Inlet/Isolator Model in Mach 5 Flow," *AIAA Journal,* vol. 47, no. 6, pp. 1528-1541, 2009.

[55] M. A. Di Stefano, S. Hosder and R. A. Baurle, "Effect of Turbulence Model Uncertainty on Scramjet Isolator Flowfield Analysis," *Journal of Propulsion and Power,* vol. 36, no. 1, 2020.

[56] H. E. Edgerton, "Shockwave photography of large subjects in daylight," *Rev. Sci. Instruments,* vol. 29, pp. 171-172, 1958.

[57] Stanford Research Systems , *MODEL DG535 Digital Delay / Pulse Generator,* Sunnyvale, CA: Stanford Research Systems, 2000.

[65] replace, arms control today.

VITA

Katherine M. Stamper was born in Chattanooga, TN in 1996 to Kelvin and Jessica Stamper. Katherine attended The University of Tennessee Knoxville where she received her Honors Aerospace Engineering degree from the Chancellor's Honors Program in 2017. After graduation, she interned at the University of Tennessee Space Institute and was subsequently brought on as a Graduate Research Assistant under Dr. John Schmisseur. She also interned with NASA Ames Research Center in 2019. She has two cats, Rey and Finn, who have kept her company throughout long writing sessions. She has also been very active in the local dance and theater community.